Научном већу
Института за физику у Београду

Предмет: **Молба за покретање поступка за стицање звања истраживач сарадник**

С обзиром да испуњавам критеријуме прописане од Министарства просвете, науке и технолошког развоја Републике Србије за стицање звања истраживач сарадник, молим Научно веће Института за физику у Београду да покрене поступак за мој избор у наведено звање.

У прилогу достављам:

1. Мишљење руководиоца пројекта са предлогом чланова комисије за избор у звање;
2. Стручну биографију;
3. Списак објављених радова и других публикација разврстан по важећим категоријама прописаним од Министарства;
4. Копије објављених радова и других публикација;
5. Потврду о уписаним докторским студијама;
6. Потврду о просеку на основним и мастер студијама;
7. Преглед научне активности;

У Београду,
21. априла 2017. године

С поштовањем,

Миљан Дашић

Научном већу Института за физику у Београду

Београд, 20. април 2017. године

Предмет: **Мишљење руководиоца пројекта о избору Миљана Дашића у звање истраживач сарадник**

Миљан Дашић је запослен у Лабораторији за примену рачунара у науци, у оквиру Националног центра изузетних вредности за изучавање комплексних система Института за физику у Београду и ангажован је на пројекту основних истраживања Министарства просвете, науке и технолошког развоја Републике Србије ОН171017, под називом "Моделирање и нумеричке симулације сложених вишечестичних физичких система". На поменутом пројекту ради на темама из моделирања динамичког понашања просторно ограничених диполних и јонских система под руководством др Игора Станковића. С обзиром да испуњава све предвиђене услове у складу са Правилником о поступку, начину вредновања и квантитативном исказивању научноистраживачких резултата истраживача МПНТР, сагласан сам са покретањем поступка за избор Миљана Дашића у звање истраживач сарадник.

За састав комисије за избор Миљана Дашића у звање истраживач сарадник предлажем:

(1) др Игор Станковић, виши научни сарадник, Институт за физику у Београду
(2) др Игор Франовић, научни сарадник, Институт за физику у Београду
(3) проф. др Сунчица Елезовић-Хаџић, редовни професор Физичког факултета Универзитета у Београду

Руководилац пројекта ОН171017

др Антун Балаж
научни саветник

Научном већу Института за физику у Београду
Београд, 21. април 2017. године

Кратка стручна биографија

Миљан Дашић рођен је 03.11.1990. године у Параћину, Србија. Завршио је ОШ „Момчило Поповић-Озрен“ и природно-математички смер Гимназије у Параћину, обе као ученик генерације и носилац Вукове дипломе. Награђиван је специјалним дипломама за српски језик и књижевност, математику, физику, хемију и програмирање, за остварене резултате на такмичењима.

Дипломирао је 5. јула 2013. године на Одсеку за Физичку Електронику Електротехничког факултета Универзитета у Београду, са просечном оценом 9.93. Свој дипломски рад урадио је у Лабораторији за нанофотонске системе Универзитета Колорадо (Сједињене Америчке Државе), под менторством проф. др Милоша Поповића. У току студија стручно се усавршавао на иностраним универзитетима: 2011. године три месеца је радио на Тиндал институту у Ирској, у оквиру UREKA 2011 летње научне праксе; потом је 2012. године четири месеца радио на Колорадо Универзитету у Сједињеним Америчким Државама, као истраживач сарадник у Лабораторији за нанофотонске системе; у 2013. години, у оквиру IAESTE стручне праксе, три месеца је радио на Лапенранта Технолошком Универзитету у Финској, у Лабораторији за физику.

Мастер студије завршио је 16. јула 2014. године, на Одсеку за Физичку Електронику Електротехничког факултета Универзитета у Београду, са просечном оценом 10.00. Свој мастер рад урадио је у Лабораторији за примену рачунара у науци на Институту за физику у Београду, под менторством др Игора Станковића.

Октобра 2014. године уписује докторске студије на Физичком факултету Универзитета у Београду, на смеру Физика кондензоване материје и статистичка физика. Од новембра 2014. године запослен је у Лабораторији за примену рачунара у науци Института за физику у Београду, на пројекту Министарства просвете, науке и технолошког развоја Републике Србије ОН171017 “Моделирање и нумеричке симулације сложених вишечестичних физичких система”. На том пројекту ради под менторством др Игора Станковића, а руководилац пројекта је др Антун Балаж. Реализовао је стручну праксу у Одељењу за напредне технологије (Advanced Technology Division) Техничког Центра компаније Тојота Мотор Европа, са седиштем у Завентему (Белгија) у периоду од 5. октобра 2015. до 8. априла 2016. године.

Добитник је више награда на домаћем и међународном нивоу. Најмлађи је учесник регуларног дела међународне конференције ТЕЛФОР 2012, одржане новембра 2012. године у Сава центру у Београду. Тада је, као студент четврте године основних студија, презентовао рад у регуларној сесији. Освојио је друго место на тимском такмичењу у студији случаја на локалном инжењерском такмичењу (LEC - Local Engineering Competition), марта 2012. у Београду. Освојио је треће место на тимском такмичењу у бизнис идејама, на Academy of Modern Management (AMM), децембра 2012. у Београду. Награђен је за најбољи рад на 7. међународној IEEESTEC конференцији, одржаној новембра 2014. године на Електронском факултету у Нишу. Носилац је стипендије Фонда за младе таленте (Доситеја) за школску 2012/2013 и 2013/2014 годину. Изабран је за члана клуба СУПЕРСТЕ за 2014. годину, у области природних наука. То је годишњи конкурс ЕРСТЕ банке, са циљем подршке младим талентима Србије.

До сада је објавио два рада у врхунским међународним часописима (М21 категорије).

Научном већу Института за физику у Београду
Београд, 21. април 2017. године

Списак научних радова

- Радови објављени у врхунским међународним часописима (M21):

1. I. Stanković, M. Dašić and R. Messina,
“Structure and Cohesive Energy of Dipolar Helices”,
Soft Matter (2016) Royal Society of Chemistry, ISSN: 1744-683X
Импакт фактор = 3.798

2. Konstantinos Gkagkas, Veerapandian Ponnuchamy, M. Dašić and I. Stanković,
“Molecular dynamics investigation of a model ionic liquid lubricant for automotive applications”,
Tribology International (2016) Elsevier, ISSN: 0301-679X
Импакт фактор = 2.259

- Саопштења са међународног скупа штампана у целини (M33):

1. M. Dašić,
“Calculation of Geometrical Packing and Binding Energy of Self-Assembled Magnetic Tubular Structures”,
INFOTEH, 18-20 March 2015, Jahorina, Bosnia and Herzegovina

- Саопштења са међународног скупа штампана у изводу (M34):

1. M. Dašić and I. Stanković,
“Theoretical and Experimental Study of Helices Composed of Spherical Dipoles”,
The 19th Symposium on Condensed Matter Physics – SFKM 2015, 7-11 September 2015, Belgrade, Serbia

Soft Matter

PAPER

View Article Online
View Journal

Cite this: DOI: 10.1039/c5sm02774h

Structure and cohesive energy of dipolar helices

Igor Stanković,*[a] Miljan Dašić[a] and René Messina[b]

Received 11th November 2015,
Accepted 18th January 2016

DOI: 10.1039/c5sm02774h

www.rsc.org/softmatter

This paper deals with the investigation of cohesive energy in dipolar helices made up of hard spheres. Such tubular helical structures are ubiquitous objects in biological systems. We observe a complex dependence of cohesive energy on surface packing fraction and dipole moment distribution. As far as single helices are concerned, the lowest cohesive energy is achieved at the highest surface packing fraction. Besides, a striking non-monotonic behavior is reported for the cohesive energy as a function of the surface packing fraction. For multiple helices, we discover a new phase, exhibiting markedly higher cohesive energy. This phase is referred to as ZZ tube consisting of stacked crown rings (reminiscent of a pile of zig-zag rings), resulting in a local triangular arrangement with densely packed filaments parallel to the tube axis.

1 Introduction

Particles with permanent dipole moments, such as magnetic particles, are well known for their outstanding self-assembly properties.[1–3] In biology, tubular and helical structures are relevant self-assembled objects, for instance, found in bacterial flagella[4] and microtubules.[5,6] Other instances of such tubular/helical structures can be found in various materials with specific building units that can be: carbon atoms,[7] coiled carbon nanotubes,[8] DNA,[9] nanoparticles,[10] or amphiphilic molecules.[11–13] Self organization of cubic magnetic nanoparticles[14] and asymmetric colloidal magnetic dumbbells[15] into helical architectures were recently reported without the need for pre-existing templates.

On a more theoretical side, hard spherical particles confined in narrow cylinders spontaneously assemble into helical structures[16,17] and this is also seen experimentally.[18] Hard-spheres with permanent moment can be employed as a paradigm for more complex helical molecular superstructures,[19] or microtubules.[20,21] The pioneering theoretical work of Jacobs and Bean[22] and later that of de Gennes and Pincus[23] shed some light on the microstructure of self-assembled unconstrained (spherical) dipoles. More recently, the paper[24] advocated the ground states of self-assembled magnetic structures. The authors proved that for a sufficiently high number of particles the ground state is obtained *via* ring stacking into tubes.[24] On the other hand, Vella *et al.*[25] showed an illustrative example in which a macroscopic straight portion of the chain spontaneously wraps itself building a tube. At larger scales, the Janus chain model was able to reproduce well the formation of superstructures and double helical conformations of amphiphilic molecules.[26,27] The competition between toroidal and rod-like conformations, as possible ground states for DNA condensation, was studied using a polymer chain model function of stiffness and short range interactions.[28,29] Also the recently introduced polymorphic dynamics model[30,31] was able to reproduce the behavior of the microtubule lattice based on a rough understanding of underlying atomic level processes. The general scientific problem of understanding the processes by which building blocks (dipoles) self-assemble and obtain their functionality is highly challenging.[32–36]

The goal of this paper is to address the intimate link between microstructure and cohesive energy. Tubular helical structures can be obtained either (i) through ring stacking or (ii) by rolling one or multiple helices on a confining cylindrical surface (Section 2). The dipolar interaction model is introduced and a link between the dipole distribution and the microstructure is established in Section 3. In Section 4, starting from the most simple case corresponding to a single helix, we discuss the relationship between the surface packing and the resulting macroscopic properties such as the cohesive energy or overall polarization. Then, the more complex situation of multiple helices with densely packed constitutive particles is addressed. There, the degree of alignment (especially in the ground state) between the dipole moment orientation and the helix axis is analyzed.

2 Geometry of helices

2.1 Geometry of the single helix

In the framework of this paper, helices are composed of hard spherical particles and confined to a cylinder's surface, *i.e.*, the helices are created by rolling threads on the cylindrical surface of radius R_{cyl}. Geometrical parameters that define a single helix are: the azimuthal angular shift Γ between the centers of two

[a] Scientific Computing Laboratory, Institute of Physics Belgrade, University of Belgrade, Pregrevica 118, 11080 Belgrade, Serbia. E-mail: igor.stankovic@ipb.ac.rs
[b] Institut de Chimie, Physique et Matériaux (ICPM), Université de Lorraine, 1 Bd. Arago, 57070 Metz, France

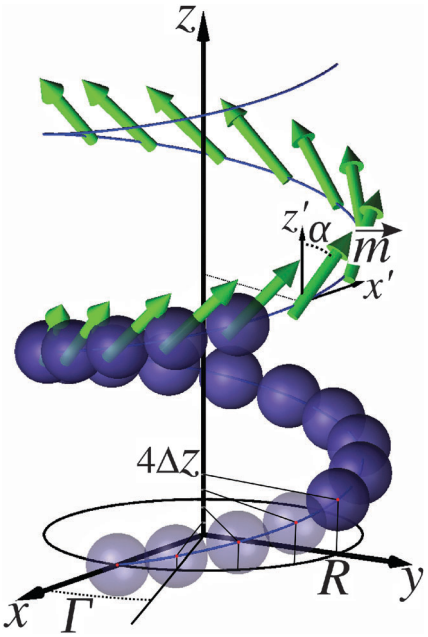

Fig. 1 Illustration of a single helix with the relevant geometrical parameters (R,Γ,Δz) labelled. The bold line connecting spherical particle centers represents the backbone of the helix. In the upper part of the figure, the azimuthal dipole moment orientation α is defined in a local coordinate system with its origin corresponding to the particle center. The z'-axis is parallel to the cylinder axis.

successive particles and the radius of the helix $R = R_{cyl} + d/2$, where d stands for the hard sphere diameter, see Fig. 1. The radius R represents physically the distance of the closest approach between the cylinder axis and the center of the spherical particle.

The Cartesian coordinates of particle i in a single helix are calculated as: $x_i = R\cos(i\Gamma)$, $y_i = R\sin(i\Gamma)$, and $z_i = i\Delta z$, where $i \in Z$ and assuming that one particle is at $(x,y,z) = (R,0,0)$. The distance between the centers of each two successive particles along the helix axis is labelled Δz, see Fig. 1. When constructing a helix, its radius R and the azimuthal angular distance Γ have to be chosen in a way that ensures non-overlapping of hard spheres. The non-overlapping constraint is expressed for any two particles i, j as $|\overleftarrow{r}_{ij}| \geq d$. Since the helix thread is connected everywhere, any two successive particles are touching. We can obtain Δz as a function of other two variables: $\Delta z = \sqrt{d^2 + 2(\cos\Gamma - 1)R^2}$. Thereby, variables Δz, R and Γ are not independent. Clearly, with decreasing Δz (*i.e.*, increasing Γ) helices become more compact. Because of the connectivity, every particle in a helix has at least two neighbors, *i.e.*, the coordination number, n_c, is always greater or equal than two ($n_c \geq 2$). The highest packing density of the particles for the prescribed confinement radius R will be achieved when the successive helix turns touch. In this situation of touching turns, the coordination number n_c can be either four or six. Therefore, in general, $n_c \in \{2, 4, 6\}$, where the case $n_c = 2$ corresponds to non-touching turns. Based on the coordination number n_c, we can classify helices as follows (see Fig. 2a–c). Examples of helices with two neighbors $n_c = 2$ and four neighbors $n_c = 4$ at a prescribed cylindrical confinement, *e.g.*, $R/d = 1.78$, are sketched in Fig. 2a and b, respectively. For a number of well-defined radii, as discussed later in this paper, densely packed helices with six neighbors ($n_c = 6$) can be formed, see Fig. 2c. In the following sections, we will also investigate stacked rings forming the so-called tubes, also depicted in Fig. 2d–f.

2.2 Order parameters for single helices

The surface packing fraction, $\eta = S/S_{avail}$, is defined as the ratio of the area $S = \pi d^2/4$ covered by one particle and the area available for one particle S_{avail}, in an unrolled configuration.

Following the definition of the surface packing density we obtain:†

$$\eta = \frac{d^2}{8\Delta z R}. \quad (1)$$

For comparison we are also going to derive the packing fraction for the tubes:‡

- The surface packing fraction of AA tubes is given by $\eta_{AA} = N_{ring}d/8R_{AA}$ for an AA tube with N_{ring} particles per ring and the confinement radius $R_{AA}/d = 1/[2\sin(\pi/N_{ring})]$, see Fig. 2d for a microstructure with $R_{AA}/d = 1.93$.

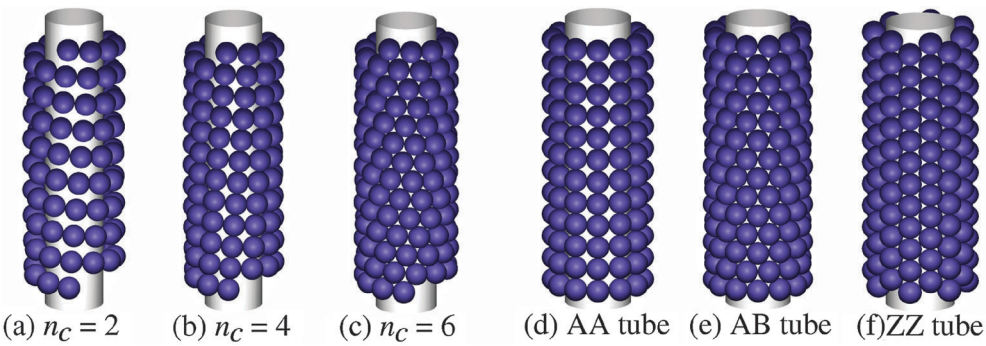

Fig. 2 Illustration of different classes of helices, based on the coordination number $n_c = 2$, 4, and 6. (a) Helix with *non-touching* turns ($n_c = 2$). (b) Helix with touching turns ($n_c = 4$). (c) Densely packed helix ($n_c = 6$). The other panels illustrate the so-called (d) AA, (e) AB, and (f) ZZ tubes. The tubes can be created by strict axial stacking of unit rings. For AA and AB tubes unit rings are flat, whereas, for ZZ tubes the unit ring has a crown shape (reminiscent of the pile of 'zig-zag' rings). The radii of AA and AB tubes are the same $R/d = 1.93$.

• Similarly, for AB tubes, the packing fraction is $\eta_{AB} = N_{ring}d^2/8R_{AB}\Delta z_{AB}$, with $R_{AB} = R_{AA}$. Here, the elevation Δz_{AB} between two consecutive rings is:

$$\Delta z_{AB} = (d/2)\sqrt{2 + 2\cos(\pi/N) - \cos^2(\pi/N)}. \qquad (2)$$

• For ZZ tubes, the packing fraction is $\eta_{ZZ} = N_{ring}d/8R_{ZZ}$, with the confinement radius $R_{ZZ}/d = \sqrt{3}/\left[4\sin\left(\pi/N_{ring}\right)\right]$.

To further characterize the helical microstructures, we introduce an additional geometrical order parameter ξ which is valid for $n_c = 4$ and 6. This order parameter connects an individual reference particle 0 located at $\vec{r}_0$ in the helix with its two neighbors: its immediate successive particle 1 in the turn ($\vec{r}_{01} = \vec{r}_1 - \vec{r}_0$) and a neighboring particle 2 from the next turn ($\vec{r}_{02} = \vec{r}_2 - \vec{r}_0$), see Fig. 3(a).

The angular coordination order parameter is conveniently defined as:

$$\xi = 2\frac{|\vec{r}_{01} \cdot \vec{r}_{02}|}{d^2}. \qquad (3)$$

In the two limiting cases, the angular coordination order parameter has values: $\xi_{min} = 0$, for a locally square lattice on a cylinder (*e.g.*, AA tubes, check Fig. 2d) and $\xi_{max} = 1$, for a locally triangular lattice (*e.g.* AB tubes, check Fig. 2e). In all other cases, the value of the angular coordination order parameter ξ is between those two extreme values, *i.e.*, $0 < \xi < 1$.

2.3 Multiple helices at high surface packing fraction

The densely packed helices ($n_c = 6$) can be created, in analogy with carbon nanotubes, by rolling a ribbon of a triangular lattice on a cylinder surface.[37] We deal with cylindrical geometry, infinite in one direction. We can generate these helical structures by periodical reproduction of a curved patch (unit cell) along the helical line with spanning vectors ($\vec{a}_1$, $\vec{a}_2$). This curved unit cell has n_1 particles along the $\vec{a}_1$ direction and n_2 particles in the $\vec{a}_2$ direction.§

Since we deal with hard spheres and we aim to build very dense structures, the parameter space (R,Δz,n_1,n_2) is significantly restricted. We are going to find out that only two of these parameters are independent. There exists a relationship linking the elevation angle $\Theta = \arcsin(\Delta z/d)$ and the confinement radius R, see ref. 37. Bearing in mind that for any pair (n_1,n_2) or equivalently (n_2,n_1), we have a unique corresponding structure

† The available area per particle is $S_{avail} = 2\pi R\Delta z$, where the distance between successive particles along the tube axis is Δz. We take for the surface covered by particle $S = \pi d^2/4$, *i.e.*, neglecting curvature. This results in a small overestimation of the packing fraction (less then 2% for large curvatures, *e.g.*, $R/d = \sqrt{3/2}$).

‡ The tubes are obtained *via* ring stacking. It is convenient to calculate the surface packing fraction as the ratio of the area covered by the particles in a unit ring and the available area per ring. The surface covered is $S = N_{ring}\pi d^2/4$. The available area per ring is $S_{avail} = 2\pi R\Delta z$, where Δz is the distance between successive rings. The distance between successive rings is $\Delta z = d$ for AA and ZZ tubes.

§ The values n_1 and n_2 can be seen as the two possible widths of the ribbon generating the same helical structure.

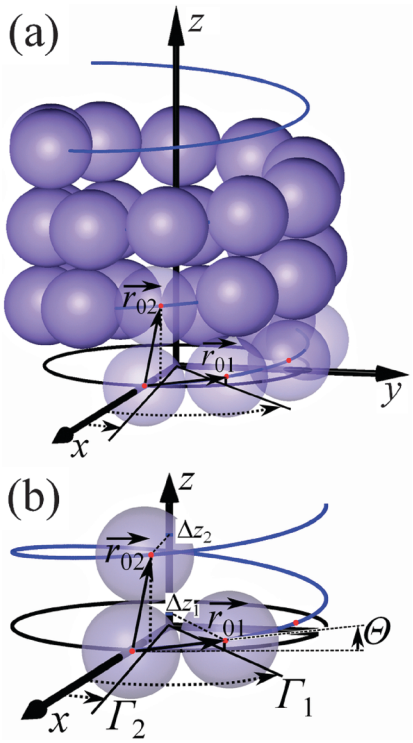

Fig. 3 (a) Illustration of a helix made of hard spheres, helix backbone (solid line), and the vectors connecting a reference particle 0 located at (x,y,z) = (R,0,0) with its neighbors: an immediate successive particle 1 in the turn located at ($\vec{r}_{01}$) and a neighboring particle 2 from the next thread turn at ($\vec{r}_{02}$). (b) An overview of the principal geometrical parameters of $n_c = 4$ and 6 helices: elevation angle Θ and azimuthal angular shifts Γ_1 and Γ_2 (see eqn (7)). In our notation, densely packed directions along the helical superstructure are called threads. The corresponding elevation distances of successive particles along helix axes $\Delta z_{1,2}$ (see eqn (9)) are also given for two possibilities for the rolling of the same helix configuration.

with $n_c = 6$, one arrives at the following two independent equations:

$$\Theta(n_1, n_2) = \arctan\left(\frac{\sqrt{3}n_2}{2n_1 + n_2}\right) \qquad (4)$$

and

$$180^\circ = n_1 \arcsin\left[\left(\frac{d}{4R}\right)\frac{2n_1 + n_2}{\sqrt{n_1^2 + n_2^2 + n_1 n_2}}\right] + n_2 \arcsin\left[\left(\frac{d}{4R}\right)\frac{2n_2 + n_1}{\sqrt{n_1^2 + n_2^2 + n_1 n_2}}\right]. \qquad (5)$$

We have solved those two equations and obtained the sets (Θ,R/d) shown in Fig. 4. For each value of R there are two different values of Θ, symmetric around $\Theta = 30^\circ$, which correspond to lattice constant pairs (n_1,n_2) and (n_2,n_1), respectively. The (n_1,n_2) pairs are actually identical structures with opposite chirality.[38] The six-fold rotational symmetry of the lattice restricts $\Theta \in [0^\circ,60^\circ]$.

We now look into properties of (n_1,n_2) pairs in order to characterize the multi-thread structure of six neighbor helices ($n_c = 6$). First, we identify the link between $n_c = 6$-tubes and the

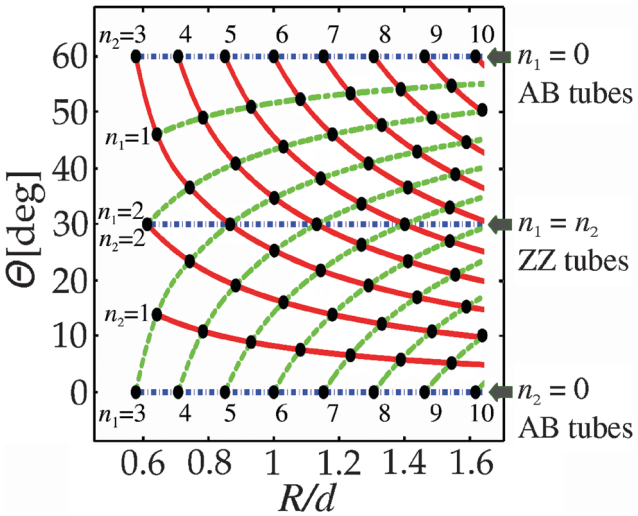

Fig. 4 Phase diagram in the (Θ,R/d)-plane showing possible unit cells characterized by (n_1,n_2) pairs. Solid lines represent unit cells with n_2 fixed, and the dashed ones represent unit cells with n_1 fixed. The three horizontal lines (dot-dashed) correspond to tubes.

(n_1,n_2) pair values. The pairs (0,n_2) and (n_1,0) leading to $\Theta = 60^\circ$ and 0°, respectively, represent AB tubes, *cf.* Fig. 4. The pairs with $n_1 = n_2$ corresponding to $\Theta = 30^\circ$ lead to ZZ tubes that are characterized by constitutive straight filaments parallel to the ZZ tube axis, see Fig. 2f. The curve with $n_1 = 1$ (with $n_2 \geq 3$) corresponds to a single helix, $n_1 = 2$ (with $n_2 \geq 3$) to a double helix, $n_1 = 3$ (for any $n_2 \geq 4$) to a triple helix, and more generally an n_1-helical structure is obtained when $n_2 \geq n_1 + 1$.¶

We employ Cartesian coordinates to express positions of particles in an n-helix similarly to the single helix case, using two indices, $i \in Z$ and $j = \{1,n\}$:

$$x_{i+jn} = R\sin(i\Gamma_1 + j\Gamma_2)$$

$$y_{i+jn} = R\cos(i\Gamma_1 + j\Gamma_2)$$

$$z_{i+jn} = i\Delta z_1 + j\Delta z_2. \quad (6)$$

In eqn (6), Γ_1 represents the azimuthal angular shift between each two consecutive particles along a given thread and Γ_2 is the angular shift between threads, *i.e.*, densely packed directions in a superstructure, see Fig. 3(b). The azimuthal angle Γ_1 is merely provided by:

$$\Gamma_1 = \arccos\left[1 - \left(\frac{d}{\sqrt{2}R}\cos\Theta\right)^2\right]. \quad (7)$$

The angular shift Γ_2 between threads is more delicate to derive. Knowing that starting from the reference particle it is possible to reach the same particle position following two paths along threads (in $\vec{a}_1$ or $\vec{a}_2$-direction), one can arrive at a relation linking Γ_1 and Γ_2: $360^\circ = (n_1 + n_2)\Gamma_1 - n_2\Gamma_2$.

The dependence of angular parameters Γ_1 and Γ_2 on the reduced helix radius R/d is displayed in Fig. 5, for $\Theta < 30$ in the single helix ($n_2 = 1$, $n_1 \geq 4$), the double helix ($n_2 = 2$, $n_1 \geq n_2$) and the quadruple helix ($n_2 = 4$, $n_1 \geq n_2$).

¶ In our notation, multiple helices are named after the smallest unit patch dimension, *i.e.*, the smallest number of generating threads.

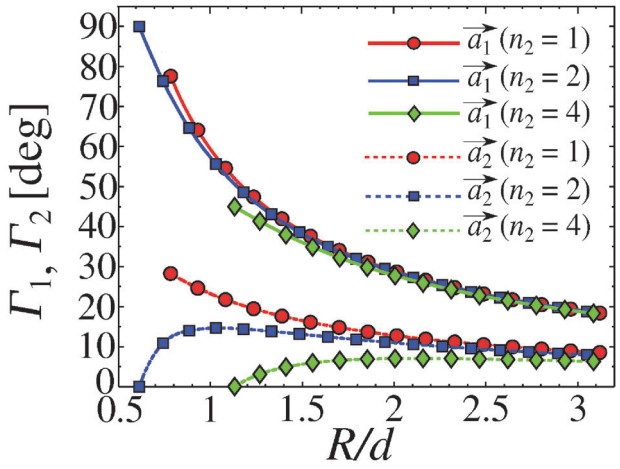

Fig. 5 Dependence of azimuthal angular shift parameters Γ_1 and Γ_2 stemming from the corresponding spanning vectors $\vec{a}_1$, $\vec{a}_2$, respectively, on a reduced helix radius R/d, for single (n_2 = 1), double (n_2 = 2), and quadruple (n_2 = 4) helices.

As the helix radius R/d increases, the value of Γ_1 monotonically decreases, since additional particles are added to a turn. The angular parameter Γ_2 monotonically decreases only for $n_2 = 1$. The scenario becomes qualitatively different at $n_2 \geq 2$ where non-monotonic behavior is found, see Fig. 5. This feature can be rationalized as follows. The smallest compatible radii R with $n_2 \geq 2$ and $\Theta < 30^\circ$ are obtained when $n_1 = n_2$ (*cf.* Fig. 4) corresponding to Z tubes where $\Gamma_2 = 0$. Besides that, Γ_2 tends to zero for the vanishing cylinder curvature ($R/d \to \infty$). These are the reasons why the profile of $\Gamma_2(R/d)$ is non-monotonic when $n_2 \geq 2$.

The surface packing fraction of densely packed multiple helices is simply obtained by multiplying the surface packing fraction of a single helix with the number of threads n_2 ($\eta_{\text{multi}} = n_2\eta$, see eqn (1)):

$$\eta_{\text{multi}} = n_2\frac{d^2}{8\Delta z_1 R}, \quad (8)$$

where the elevation distance Δz_1 (shown in Fig. 3b) is given by:

$$\Delta z_1 = \sqrt{d^2 - 4R^2\sin^2\left(\frac{\Gamma_1}{2}\right)}. \quad (9)$$

The calculated surface packing fraction of single (n_2 = 1), double (n_2 = 2), and quadruple (n_2 = 4) helices is shown in Fig. 6. At a given confinement curvature (fixed R/d), adding threads results in higher surface packing fraction, see Fig. 6.

3 Dipole moments

3.1 Dipolar interaction model

We now want to address the situation where the constitutive particles are dipolar. Each particle carries an identical dipole moment in magnitude, $m = |\vec{m}_i|$, where $\vec{m}_i = (m_i^x, m_i^y, m_i^z)$ defines

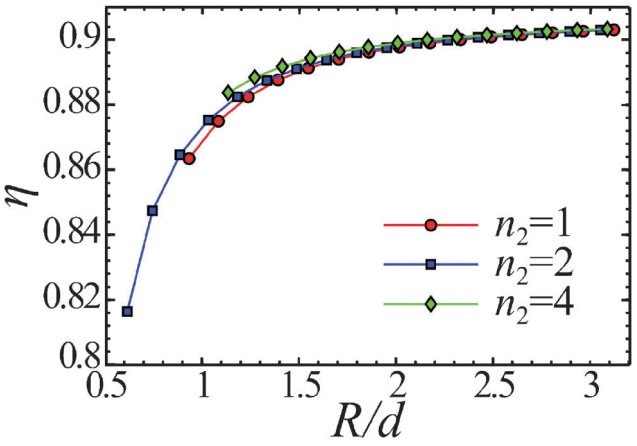

Fig. 6 Surface packing fraction η, see eqn (8) as a function of reduced helix radius R/d for single (n_2 = 1), double (n_2 = 2), and quadruple (n_2 = 4) helices.

the dipole moment of particle i, see also Fig. 1. The potential energy of interaction $U(\vec{r}_{ij})$ between two point-like dipoles whose centers are located at $\vec{r}_i$ and $\vec{r}_j$ can be written as:

$$U(\vec{r}_{ij}) = C\frac{1}{r_{ij}^3}\left[\vec{m}_i \cdot \vec{m}_j - 3\frac{(\vec{m}_i \cdot \vec{r}_{ij})(\vec{m}_j \cdot \vec{r}_{ij})}{r_{ij}^2}\right] \quad (10)$$

for $r_{ij} \geq d$ or ∞ otherwise, where C represents a constant that depends on the intervening medium, and $r_{ij} = |\vec{r}_{ij}| = |\vec{r}_j - \vec{r}_i|$. It is convenient to introduce the energy scale defined by $U_{\uparrow\uparrow} \equiv Cm^2/d^3$ that physically represents the repulsive potential value for two parallel dipoles in contact standing side by side as clearly suggested by the notation. Therefore, the total potential energy of interaction in a given structure U_{tot} is given by

$$U_{\text{tot}} = \sum_{\substack{i,j \\ i>j}} U(\vec{r}_{ij}). \quad (11)$$

One can then define the reduced potential energy of interaction u (per particle) of N magnetic spheres. It reads $u = U_{\text{tot}}/(U_{\uparrow\uparrow}N)$, which will be referred to as the cohesive energy.

Since we are dealing with infinitely long structures (in one direction), we shall consider only periodic structures in that direction that greatly facilitate the calculation of the cohesive energy. The method of choice is provided by the Lekner sum for systems with periodicity in one direction.[39] The central feature in the Lekner method is the choice of the periodic cell. For n_c = 2, 4, we can always find helical parameters with a finite number of particles in the unit cell. The periodicity is achieved by imposing a condition on the angular shift parameter Γ that a helix has to make an integer number of turns within the unit cell.

3.2 Dipole moment orientation prescribed by helix threads

Because of the symmetry it is intuitive to envision dipole moments following helix threads. In order to have dipole moments tangential to the helical backbone, we introduce two components of dipole moments. The parallel component with respect to the helix axis is given by $m^z = m\Delta z/d$ and the orthogonal one is given by $|\vec{m}^{xy}| = m\sqrt{1-(\Delta z/d)^2}$. Hence, the dipole moment of particle i in the single thread helix reads: $m_i^x = -m^{xy}\sin(i\Gamma)$, $m_i^y = m^{xy}\cos(i\Gamma)$, and $m_i^z = m_z$.

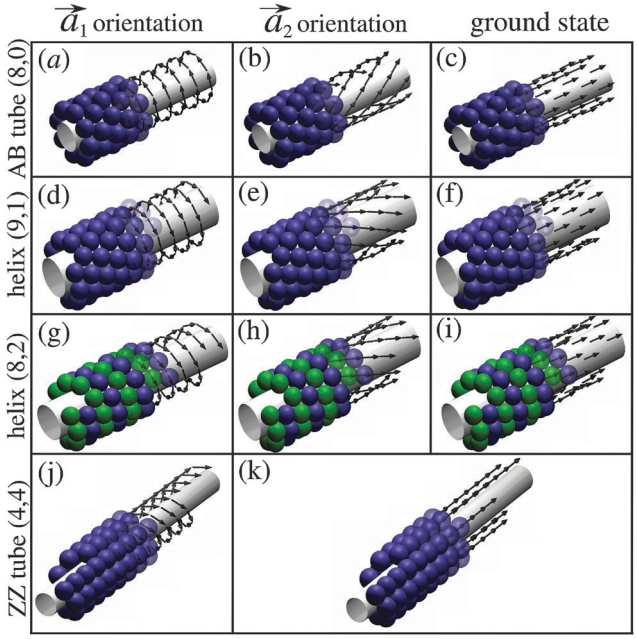

Fig. 7 The representative structures including dipole moment distributions are displayed. For AB tubes with patch parameters (n_1,n_2) = (8,0) dipole distributions which correspond to spanning unit cell vectors (a) $\vec{a}_1$ (oblique to cylinder's axis), (b) $\vec{a}_2$ (closer to cylinder's axes), and (c) ground state dipole distribution. For a single helix (n_1,n_2) = (9,1) dipole distributions which correspond to (d) $\vec{a}_1$ and (e) $\vec{a}_2$ (closer to helix axes) spanning vectors, and(f) ground state dipole distribution. For a double helix (n_1,n_2) = (8,2) dipole distributions which correspond to (g) $\vec{a}_1$, (h) $\vec{a}_2$ (closer to helix axes) spanning vectors, and (i) the ground state dipole distribution. In the case of ZZ tubes (j) $\vec{a}_1$ and (k) $\vec{a}_2$ dipole distributions are shown. The ground state of ZZ tubes follows $\vec{a}_2$ dipole distribution (parallel to cylinder's axis).

In the multi-thread case, the Cartesian dipole moment components are given by:

$$m_{i,j}^x = -m^{xy}\sin(i\Gamma_1 + j\Gamma_2)$$

$$m_{i,j}^y = m^{xy}\cos(i\Gamma_1 + j\Gamma_2)$$

$$m_{i,j}^z = m\Delta z/d, \quad (12)$$

where $i \in Z$ is the internal particle label within a thread and $j = \{1,n_2\}$ stands for the thread's label. In dense helices (n_c = 4, 6) dipole moments can follow two directions $\vec{a}_1$ and $\vec{a}_2$. In Fig. 7, representative dipole moment distributions are shown.

3.3 Energy minimization

In general, the dipole moments do not have to follow thread structure. To find the dipole moment distribution that yields minimal energy, we first perform minimization of the cohesive energy using a constrained minimization algorithm.[24,40] A randomly oriented dipole moment is assigned to every particle of the helical structure in the following way: dipole moment is defined in the spherical coordinate system. Two important features stemming from these energy minimization calculations are:

(i) Dipole moments are tangential to the cylinder's surface.

(ii) The component of dipole moment in the z-axis direction m_z for a given structure is identical for all particles.‖

Therefore we need just one angular parameter to characterize the dipole moment orientation. We choose the dipole moment angular parameter, $\alpha \in [-180^\circ, 180^\circ]$, relative to the z-axis, see Fig. 1. Doing so we arrive at:

$$m^x_{i,j} = -m\sin(\alpha)\sin(i\Gamma_1 + j\Gamma_2)$$

$$m^y_{i,j} = m\sin(\alpha)\cos(i\Gamma_1 + j\Gamma_2)$$

$$m^z_{i,j} = m\cos(\alpha), \qquad (13)$$

where the indices i and j have the same meaning as in eqn (12). Consequently, the angular parameter α is most of the time a unique variable, at prescribed helical structures, entering into the energy minimization routine.

4 Cohesion energy and microstructure

4.1 Compression of a single helix

A simple way to deform a helix is to compress (or extend) it along its axis, *i.e.*, the z-direction, while ensuring the dipole moments follow the thread (for details of implementation, see Section 3.2). Compression of a helix results in a continuous increase of its surface packing fraction η. Fig. 8 shows the evolution of cohesive energy u_R with the surface packing fraction η for a single helix with reduced radius ($R/d \simeq 1.7$, chosen in the vicinity of $n_c = 6$ point). Recalling geometrical considerations in Section 2.1 the increase of the azimuthal angular shift Γ at prescribed curvature results in a continuous decrease of Δz and compression of the helix. The compression process begins with a fully extended helix (*i.e.*, $\eta \to d/8R \approx 0.073$) where the chain stands up with $\Delta z/d = 1$, and the cohesive energy of infinite chain $u \simeq -2.404$.[24] The compression ends when two successive turns of the helix touch, *i.e.*, the coordination number of particles in the helix changes from $n_c = 2$ to $n_c = 4$.

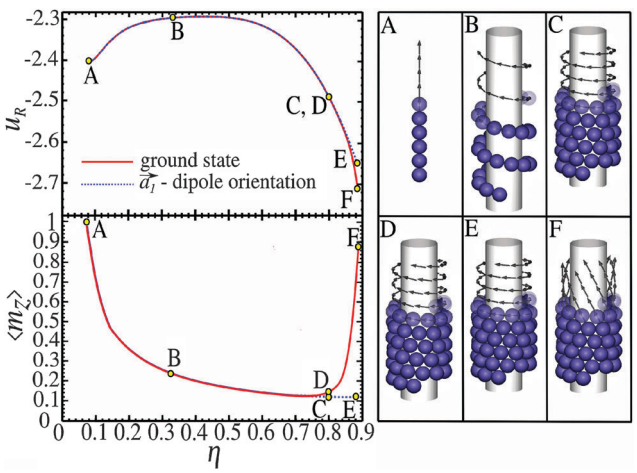

Fig. 8 Compression of a single helix on a cylindrical confinement with a fixed radius ($R/d \simeq 1.7$). Dependence of cohesive energy (upper left panel) and the overall polarization order parameter, *i.e.*, the axial component of the dipole moment (in lower left panel), on the packing fraction is shown for two characteristic dipole moment orientations: one that follows the helix, *i.e.*, the spanning vector $\vec{a}_1$ and the ground state dipole moment orientation obtained by energy minimization. Comparative microstructures at different η values (A–F) are depicted on the right panel. Configurations (A, B, C and E) correspond to a dipole moment distribution following the helix whereas configurations D and F correspond to ground state distributions.

We also address the minimal energy of the helix with respect to the dipole moment distribution (*i.e.*, not necessarily prescribed by tangentially following the helix). From Fig. 8, we observe that $u_R = u_R(\eta)$ is non-monotonic. We can identify two regimes:

- At small packing fractions up to $\eta \lesssim 0.4$ (with no touching turns), the compression of the helix requires energy input and therefore cohesive energy increases. The reason for this is that two distant consecutive turns of the helix experience weaker attraction upon increasing η.
- In the regime of high $\eta \gtrsim 0.4$ where successive turns are allowed to be close or even touching, the cohesive energy starts to decrease as η increases, *i.e.*, the helix would compress on its own without input of energy. This is a consequence of enhanced attraction caused by the discreteness of the constitutive dipolar beads, see ref. 41.

The overall polarization order parameter $\langle m_z \rangle$ is also analysed in Fig. 8. During most of the course of the helix compression, see Fig. 8, a dipole moment orientation following the helix corresponds to the ground state structure up to $\eta \approx 0.8$, *cf.* points C and D in Fig. 8 (for details of ground state calculations, see Section 3.3). Only for very high packing fractions, *i.e.*, $\eta > 0.8$, the ground state dipole orientation starts to rapidly deviate from the helix direction accompanied by a significant reduction in cohesive energy (see points E and F in Fig. 8). The highest difference in $\langle m_z \rangle$ occurs for $\eta \approx 0.887$, where $n_c = 4$ helix with touching turns is formed, and the energy difference $u_R^E - u_R^F \simeq 0.06$.

4.2 From the square to triangular arrangement for a single helix

Having successfully parameterized helices and introduced dipole moments, it is natural to ask how cohesive energy depends on structural changes and especially on curvature. With increasing curvature the structure will change from the triangular to square arrangement and *vice versa* through a continuous series of rhombic configurations. We first study in detail systems with dipole moments following the spanning vector that are most oblique to helix axes, see Fig. 7d. For the sake of comparison with tubes (AA/AB tubes), we also chose dipole moments that are building vortices along the rings for them, *cf.* Fig. 7a. Motivation for that choice stems from a previous study,[24] where we have shown that finite AB tubular systems are energetically favorable, see Fig. 7a (dipole moment orientation is perpendicular to the tube's axis).

The surface packing fraction η (eqn (1)), the angular coordination order parameter ξ (see eqn (3)), and the cohesive energy per particle u_R (eqn (11)) are plotted *versus* the reduced helix radius R/d in Fig. 9.

‖ We have found that under some circumstances the dipole moment orientations alternate, *i.e.*, antiferromagnetic-like coupling between the neighboring threads. This actually occurs with any AA tube. Similar behavior is reported for some moderately dense $n_c = 4$-helical structures.

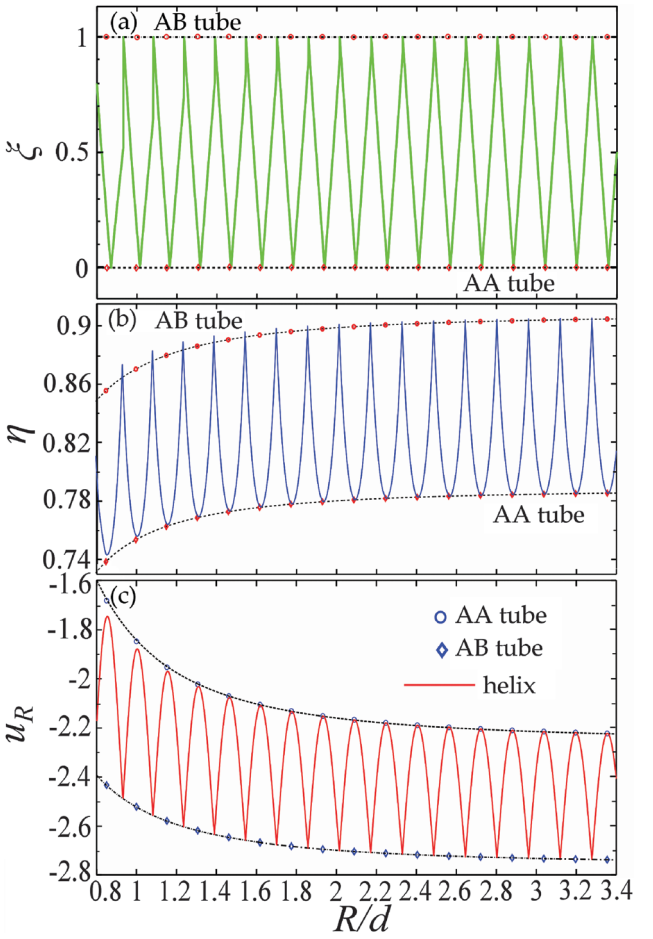

Fig. 9 Dependence of (a) the angular coordination order parameter ξ, (b) the packing density η and (c) the cohesive energy u_R on the helix radius R/d, for $\vec{a}_1$ dipole orientation. AA and AB tube points are clearly indicated, they bracket the parameter values of helices, like a kind of envelope (solid and dashed lines connecting the tube points are power law fits).

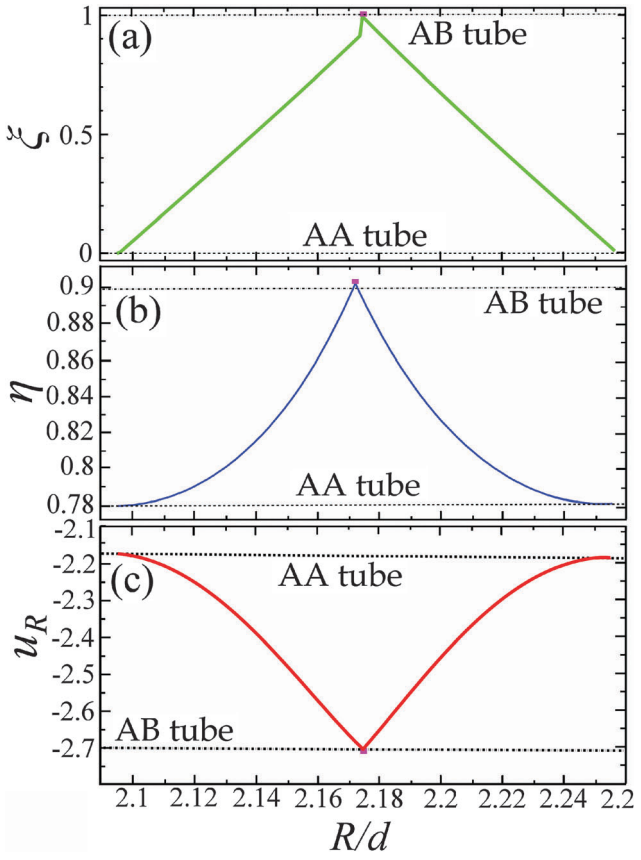

Fig. 10 Dependence of (a) the angular coordination order parameter ξ, (b) the packing density η and (c) the cohesive energy u_R on the helix radius R/d, for a segment in the vicinity of $R_{(13,1)}/d = 2.17$ of Fig. 9. Tubes AA and AB are represented by discrete points since they can be formed only with a fixed number of particles in a ring, the fitted (power law) curves serve only as a guide to the eye. The point which represents the dense helix with $(n_1,n_2) = (13,1)$ and $R_{(13,1)}/d = 2.17$ is marked with a rectangle.

Actually, the energy and structural properties change in an oscillatory quasi-periodic manner and they are enveloped from both sides with the properties of AA and AB tubes, see Fig. 9. In Fig. 10 behavior of these observables is depicted within one period ($R/d \in [2.09,2.26]$, arbitrary chosen). In one period, the number of particles (n) in a constitutive ring of (AA/AB) tubes is increased for one, *i.e.*, from n-ring to $n + 1$-ring. Within this period, the order parameter changes from $\xi = 0$, *i.e.*, square arrangement, to $\xi = 1$, *i.e.*, triangular arrangement, *via* a continuous rhombic transformation, see Fig. 10a. The radii of densely packed helices are roughly in the middle between two corresponding (AB/AA) tube radii, see Fig. 10a. This is a result of the radial constraint and the excluded volume. Though in a single thread helical structure we cannot close rings in the plane perpendicular to the cylinder axis, one can nevertheless realize a full 360° helix turn with roughly $n + 1/2$ particles. We observe discontinuity and strong asymmetry of the angular coordination order parameter ξ at the mid-period ($R_{(13,1)}/d \approx 2.17$), see Fig. 10a. This is due to a change in the number of lateral threads n_2, see Fig. 7e for illustration, at the mid period going from $n_2 = 9$ to $n_2 = 10$, see Fig. 10a.

With decreasing curvature, the surface packing fraction increases globally, see Fig. 9b. We observe oscillatory behavior as the system continuously evolves from the square to triangular arrangement and *vice versa*. The AA and AB tubes still roughly bound have the values taken by the surface packing fraction. At the helix radius $R/d > 3.4$, see Fig. 9b, we are already within 3% of the asymptotic expected values in the planar case. In contrast to the angular coordination parameter ξ, the surface packing density η is continuous everywhere, compare Fig. 10a and b. Moreover, at mid-period the η value is slightly (and systematically, see Fig. 9b) above the interpolated stemming from AB tubes (see Fig. 10b). In Fig. 9b and c, it can be clearly seen that the profiles of energy oscillations u_R and the surface packing fraction η are anti-correlated. The mid-period values u_R coincide with interpolated stemming from AB tube radii (confirmed by Fig. 9c and 10c).

4.3 Looking for the ground state

At this point, we would like to discuss mechanisms which govern the minimal energy dipole moment orientation near the mid-period transition point (more details about implementation are provided in Section 3.3). There are three privileged directions in

a helix: two which follow helix spanning vectors (determined by $\vec{a}_1$, $\vec{a}_2$) and the third one which is the direction of the helix axis. These privileged directions come into play in two competing mechanisms:

• The first mechanism is typically dictated by first neighbor interactions which favor dipole moments following the thread directions.

• The distant–neighbor interactions favor the distribution of dipole moments parallel to the helix axis.

We can justify these two mechanisms as follows. It is well known for a small finite system that rings are formed with dipole moments building vortices, *cf.* ref. 24. When a helix turn is projected along the *z*-axis, the resulting figure is highly reminiscent of the vortex discussed above. The head to tail configuration is favored at long distances, explaining the second advocated mechanism.

The abrupt change in polarization (or magnetization) in the direction of the axis $\langle m_z \rangle$, seen in Fig. 11b, is correlated with the discontinuous change in the angular coordination order parameter ξ in the vicinity of transition, see Fig. 10a. At the mid-period point $R_{(13,1)}/d = 2.17$ magnetization in the direction of the axis $\langle m_z \rangle$ is close to one, but not exactly one, see Fig. 11.

For the sake of comparison with tubes (AA/AB tubes), we choose dipole moments that are parallel with the helix axis, see Fig. 7c. The fact that the system is able to relax its dipole moment orientation to the ground state results in more dependence of energy on confinement curvature around the mid-point. The degree of asymmetry of u_R is stronger around the transition point, see Fig. 11b, than in the excited state in Fig. 10c. The ground state calculations confirm the high stability of AB tubes (see Fig. 10c).

4.4 Cohesion energy for multiple helices at high surface packing fraction

In this part, we consider the high surface packing fraction regime with $n_c = 6$. Some representative structures including dipole moment streamlines are displayed in Fig. 7. The streamlines following spanning unit cell vectors $\vec{a}_1$ (oblique to the helix axis) and $\vec{a}_2$ (more aligned to the helix axis) are also shown.** Dipole moment distributions in the ground states are also indicated for comparison in Fig. 7. In analogy with the study of a single helix case (see Section 4.2), we start analysis with a dipole moment distribution prescribed by tangentiality with the thread backbone. In Fig. 12, cohesive energy for the $\vec{a}_1$-generated dipole moment distribution is shown for different helical structures.

The cohesive energy in a planar triangular lattice, $u_\infty \simeq -2.759$, represents the energy value which will be reached asymptotically ($R/d \to \infty$) for all considered structures. As already found for AB tubes in ref. 24, cohesive energy exhibits the scaling law of the form $u_R - u_\infty \sim R^{-2}$, see Fig. 12. The cohesive energies of all three helices and AB tubes are weakly dependent on the number of threads for $\vec{a}_1$-generated dipole moment distribution.

** It is possible to polarize the helix by a homogeneous external field parallel to its axis. For symmetry reasons, a reversal of the magnetic field should result in the reversal of the dipole orientation. In the case of magnetic dipoles, it should also be possible to polarize the system to follow $\vec{a}_1$ and $\vec{a}_2$ spanning vectors by combination of a curling magnetic field of electric current flowing through the confining cylinder and the homogeneous external magnetic field parallel to its axis.

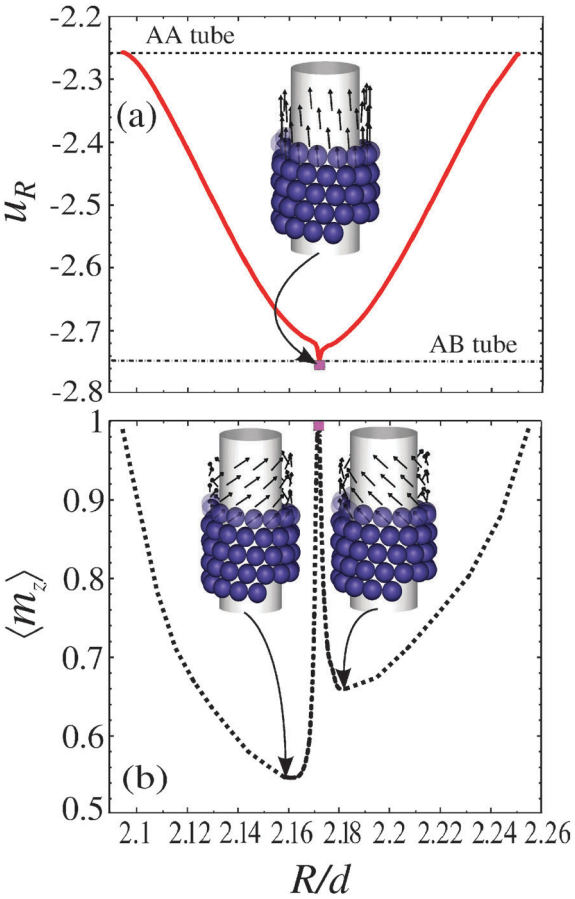

Fig. 11 Dependence of (a) cohesive energy u_R and (b) the overall polarization order parameter $\langle m_z \rangle$ on the helix radius R/d (in the ground state), for a chosen segment of Fig. 9. Tubes AA and AB are represented by discrete points since they can be formed only with a fixed number of particles in a ring, the fitted (power law) curves serve only as a guide to the eye. The point which represents the dense helix with $(n_1,n_2) = (13,1)$ and $R_{(13,1)}/d = 2.17$, is marked with a rectangle.

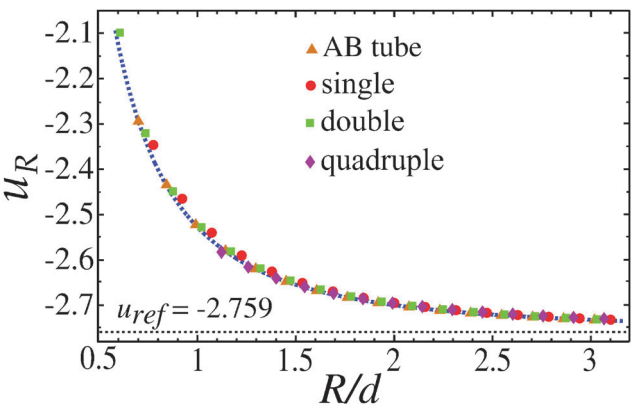

Fig. 12 Dependence of cohesive energy u_R on the helix radius R/d, for single, double, and quadruple helices at high surface packing fraction, and AB tubes, with $\vec{a}_1$ dipole orientation.

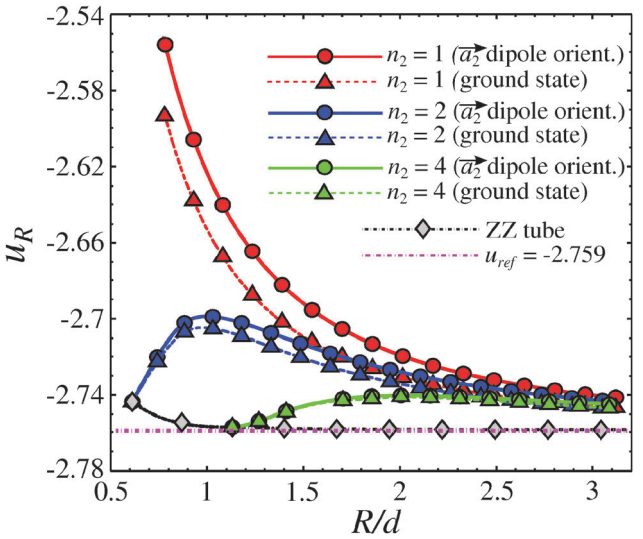

Fig. 13 Dependence of cohesive energy u_R on the helix radius R/d, for families of single, double, and quadruple helices at a high surface packing fraction, *i.e.*, $n_2 = \{1, 2, 4\}$, respectively, and AB tubes, with $\vec{a}_2$ and optimized dipole moment orientation.

This is in accordance with surface packing fraction behavior reported in Fig. 6. A comparison with the azimuthal angular shift parameter Γ_1, see Fig. 5, and the corresponding cohesive energy (for $\vec{a}_1$-generated dipole moment distribution) clearly reveals a correlation between these two quantities.

In Fig. 13, cohesive energy for $\vec{a}_2$-generated dipole moment distribution is compared with ground state energy for a different number of threads. There exists an analogous correlation (as discussed for $\vec{a}_2$-dipole distribution) between the azimuthal shift Γ_2 and the resulting cohesive energy, compare Fig. 5 and 13.

The smallest compatible radius R for multi thread helices (n_2 = 2, 4) is obtained for ZZ tubes ($n_1 = n_2$). In Fig. 13, the corresponding radii read $R_{(2,2)}/d$ = 0.61 and $R_{(4,4)}/d$ = 1.13. In this case the $\vec{a}_2$ and ground state dipole moment orientations are the same, see Fig. 7k. Strikingly, ZZ tube ground states converge very fast to the expected planar value u_∞ at the smallest accessible radii, *i.e.*, the largest curvature, within less than 1% of the planar case, see Fig. 13 for $R_{(2,2)}/d$ = 0.61. A structural similarity of ZZ tubes, with typical experimental images of microtubules is striking, see Fig. 7k. Structurally, ZZ tubes can be created by closing the rectangular strip on a cylinder and decomposition into chains which are analogous to biological filaments which the microtubules are made of.

5 Conclusions

We have presented a study about cohesive energy of helical structures composed of hard spheres with permanent dipole moments. Helices were created by replication of a particle or patch (of particles) on a confining cylindrical surface. Even for the most simple situation, namely the single thread helix, a non-trivial behavior is found when monitoring the cohesive energy as a function of surface packing (*i.e.*, axial compression). In particular, we observe a non-monotonic dependence of the cohesive energy on the packing fraction (or equivalently the amount of compression) as a result of a delicate interplay of dipole–dipole interactions and excluded volume effects. The lowest cohesive energy is achieved at the highest packing fraction with touching turns. In parallel, the magnetization (or polarization) order parameter, *i.e.*, the mean dipole moment per particle in $\langle m_z \rangle$, also exhibits a striking non-monotonic behavior as a function of the extent of compression. In the regime of very high surface packing fraction with local triangular arrangement compatible with certain cylinder radius (R) *vs.* particle diameter (d) ratio (R/d), a pronounced cohesive energy is found. Concomitantly, the magnetization order parameter indicates a sharp change in the dipole moment orientation, which tends to be parallel to the helix axis.

Finally, we compare cohesive energies of dense multiple (*i.e.*, double or quadruple) helices, as well as, AB and ZZ-tubes made up of stacking rings that can also be seen as special multiple helices. A remarkable finding is the enhanced cohesive energy for the ZZ-tube structure. The latter already emerges at strong substrate curvature with cohesive energies very close to that obtained at vanishing curvatures. In these ZZ-tube structures, an alignment of the helix threads with its axis is a microstructural signature for this low cohesive energy. As a final note, we would like to emphasize that our model mimics nicely the geometry and microstructure of microtubules. It could also provide a possible clue about the self-assembly mechanisms and cohesion within microtubular structures.

Acknowledgements

The authors acknowledge support from the bilateral Franco-Serbian PHC Pavle Savic 2014/15 Grant 32135NJ. I.S and M.D. acknowledge financial support from Ministry of Education, Science, and Technological Development of the Republic of Serbia projects ON171017 and III45018, and European Commission under H2020 projects VI-SEEM and DAFNEOX (Grant No. 675121 and 645658). Numerical calculations were run on the PARADOX supercomputing facility at the Scientific Computing Laboratory of the Institute of Physics Belgrade.

References

1 W. Wen, N. Wang, D. W. Zheng, C. Chen and K. N. Tu, *J. Mater. Res.*, 1999, **14**, 1186–1189.
2 D. J. Sellmyer, *Nature*, 2002, **420**, 374–375.
3 G. M. Whitesides and B. Grzybowski, *Science*, 2002, **295**, 2418–2421.
4 K. F. Jarrell and M. J. McBride, *Nat. Rev. Microbiol.*, 2008, **6**, 466–476.
5 I. M. Cheeseman and A. Desai, *Nat. Rev. Mol. Cell Biol.*, 2008, **9**, 33–46.
6 J. Howard and A. A. Hyman, *Nat. Rev. Microbiol.*, 2009, **10**, 569–574.
7 D. V. Kosynkin, A. L. Higginbotham, A. Sinitskii, J. R. Lomeda, A. Dimiev, B. K. Price and J. M. Tour, *Nature*, 2009, **458**, 872–876.

8 X. Zhang, X. Zhang, D. Bernaerts, G. Van Tendeloo, S. Amelinckx, J. Van Landuyt, V. Ivanov, J. Nagy, P. Lambin and A. Lucas, *EPL*, 1994, **27**, 141.
9 S. M. Douglas, J. J. Chou and W. M. Shih, *Proc. Natl. Acad. Sci. U. S. A.*, 2007, **104**, 6644–6648.
10 G. D. Lilly, A. Agarwal, S. Srivastava and N. A. Kotov, *Small*, 2011, **7**, 2004–2009.
11 T. Shimizu, M. Masuda and H. Minamikawa, *Chem. Rev.*, 2005, **105**, 1401–1444.
12 Y. Yamamoto, T. Fukushima, Y. Suna, N. Ishii, A. Saeki, S. Seki, S. Tagawa, M. Taniguchi, T. Kawai and T. Aida, *Science*, 2006, **314**, 1761–1764.
13 W. Zhuang, E. Kasemi, Y. Ding, M. Kröger, A. D. Schlüter and J. P. Rabe, *Adv. Mater.*, 2008, **20**, 3204–3210.
14 G. Singh, H. Chan, A. Baskin, E. Gelman, N. Repnin, P. Kral and R. Klajn, *Science*, 2014, **345**, 1149–1153.
15 D. Zerrouki, J. Baudry, D. Pine, P. Chaikin and J. Bibette, *Nature*, 2008, **455**, 380–382.
16 G. Pickett, M. Gross and H. Okuyama, *Phys. Rev. Lett.*, 2000, **85**, 3652–3655.
17 E. C. Oguz, R. Messina and H. Loewen, *EPL*, 2011, **94**, 28005.
18 M. A. Lohr, A. M. Alsayed, B. G. Chen, Z. Zhang, R. D. Kamien and A. G. Yodh, *Phys. Rev. E: Stat., Nonlinear, Soft Matter Phys.*, 2010, **81**, 040401.
19 A. Mershin, A. A. Kolomenski, H. A. Schuessler and D. V. Nanopoulos, *BioSystems*, 2004, **77**, 73–85.
20 E. D. Spoerke, G. D. Bachand, J. Liu, D. Sasaki and B. C. Bunker, *Langmuir*, 2008, **24**, 7039–7043.
21 M. Cifra, J. Pokorny, D. Havelka and O. Kučera, *BioSystems*, 2010, **100**, 122–131.
22 I. Jacobs and C. Bean, *Phys. Rev.*, 1955, **100**, 1060.
23 P.-G. De Gennes and P. A. Pincus, *Phys. Kondens. Mater.*, 1970, **11**, 189–198.
24 R. Messina, L. A. Khalil and I. Stanković, *Phys. Rev. E: Stat., Nonlinear, Soft Matter Phys.*, 2014, **89**, 011202.
25 D. Vella, E. du Pontavice, C. L. Hall and A. Goriely, *Proc. R. Soc. London, Ser. A*, 2013, **470**, 20130609.
26 Y. Ding, H. C. Öttinger, A. D. Schlüter and M. Kröger, *J. Chem. Phys.*, 2007, **127**, 094904.
27 M. Kröger, O. Peleg, Y. Ding and Y. Rabin, *Soft Matter*, 2008, **4**, 18–28.
28 T. X. Hoang, A. Giacometti, R. Podgornik, N. T. Nguyen, J. R. Banavar and A. Maritan, *J. Chem. Phys.*, 2014, **140**, 064902.
29 R. Cortini, B. R. Caré, J.-M. Victor and M. Barbi, *J. Chem. Phys.*, 2015, **142**, 105102.
30 H. Mohrbach, A. Johner and I. M. Kulić, *Phys. Rev. Lett.*, 2010, **105**, 268102.
31 O. Kahraman, H. Mohrbach, M. M. Müller and I. M. Kulić, *Soft Matter*, 2014, **10**, 2836–2847.
32 D. Tomanek, S. G. Kim, P. Jund, P. Borrmann, H. Stamerjohanns and E. R. Hilf, *Z. Phys. D: At., Mol. Clusters*, 1997, **40**, 539–541.
33 T. A. Prokopieva, V. A. Danilov, S. S. Kantorovich and C. Holm, *Phys. Rev. E: Stat., Nonlinear, Soft Matter Phys.*, 2009, **80**, 031404.
34 G. Pál, F. Kun, I. Varga, D. Sohler and G. Sun, *Phys. Rev. E: Stat., Nonlinear, Soft Matter Phys.*, 2011, **83**, 061504.
35 V. Malik, A. V. Petukhov, L. He, Y. Yin and M. Schmidt, *Langmuir*, 2012, **28**, 14777–14783.
36 N. Vandewalle and S. Dorbolo, *New J. Phys.*, 2014, **16**, 013050.
37 D. A. Wood, C. D. Santangelo and A. D. Dinsmore, *Soft Matter*, 2013, **9**, 10016–10024.
38 W. T. B. Kelvin, *The molecular tactics of a crystal*, Clarendon Press, 1894.
39 A. Grzybowski and A. Bróadka, *Mol. Phys.*, 2003, **101**, 1079–1088.
40 L. Assoud and R. Messina, *Phys. Rev. E: Stat., Nonlinear, Soft Matter Phys.*, 2011, **83**, 036113.
41 R. Messina and I. Stanković, *arXiv:1602.00861*, 2016.

Calculation of Geometrical Packing and Binding Energy of Self-Assembled Magnetic Tubular Structures

Miljan Dašić
Student of the the doctoral studies
Faculty of Physics, University of Belgrade
Institute of physics Belgrade
mdasic@ipb.ac.rs

Abstract—**This paper is dealing with tubular structures composed through the self-assembly of magnetic hard spheres, in a given geometric confinement. Since the structures are tubes, geometric confinement is a cylinder with a given radius (confinement radius). Interaction of interest is magnetic dipole-dipole interaction, therefore a detailed analysis of it is provided. Next step is formation of the structures. We are analyzing infinitely long tubes, therefore an efficient method (Lekner method) for summing the dipole-dipole interactions of 1D periodical systems (periodical along one direction, the z-axis) is implemented in MATLAB. One of the main goals is determination of energetically favoured configurations, so a comparison of the tubes' energy has been done.**

Key words-calculations; geometrical packing; binding energy; magnetic; tubes; MATLAB

I. INTRODUCTION

Self-assembly of magnetic particles is an interesting and relevant research topic which investigates the ways of forming regular structures composed of magnetic particles, in a fixed geometric confinement. Interaction between each two particles is magnetic dipole-dipole interaction [1]. What is a magnetic particle? It is a hard sphere which is a magnet (it has magnetic dipole moment). Why is this topic attractive? First of all, it is relevant from the theoretical point of view, since the dipole-dipole interaction is a long-ranged ($\sim 1/r^3$, r is the distance) and unisotropic interaction. Applications of magnetic structures are numerous, especially in nanoelectronics and biotechnology. For example, in nanotechnology, mixtures of self-assembled magnetic particles can lead to the formation of very strong magnets [2,3]. Interaction between magnetic planar layers can lead to 3D structures with a great potential for the microfabrication of electronic devices [4]. Ground states of microstructures in ferofluid monolayers, in which the interaction is magnetic dipole-dipole interaction, have been investigated [5]. In the paper [6] self-assembled magnetic structures with minimal energy (ground state) have been found. It has been shown that as the number of particles, N, increases, the dimensionality of the ground state structures increases as well. For a small number of particles (N = {2, 3}), a chain is the ground state. For (3 < N < 14), a chain closes into a ring. In the end, for a sufficiently big number of particles (N > 13) ground state is obtained via ring stacking. There is a clear transition with the increase of N, since a chain is 1D, a ring is 2D and stacked rings is a 3D structure. The subject of this paper is investigation of 3D structures (infinitely long tubes) formed via ring stacking into tubes. In the first part of this paper, a detailed analysis of the magnetic dipole-dipole interaction is performed, in order to better understand self-assembly of magnetic particles. There are two specific geometrical packings of the rings into tubes (square and triangular), leading to so called, AA and AB tubes. Our goal is to form a certain structure and calculate its binding energy, which is a result of the dipole-dipole interactions of each pair of particles that are building it. Once a structure is built geometrically, its dipole orientation (also called magnetization) should be defined. We have introduced three different magnetizations (ST/MT/ZZ magnetization) and compared their impact on the energy. Also, for a fixed magnetization, a scan over a wide range of confinement radii has been done, in order to understand how does the energy change when the confinement radius increases. When the confinement radius goes to infinity, then a convergence to corresponding lattice plane happens [6], which confirms the accuracy of the implemented summation method.

II. MAGNETIC DIPOLE-DIPOLE INTERACTION

Interaction for modelling the self-assembly of hard magnetic spheres is magnetic dipole-dipole interaction.
It occurs between two particles with magnetic moments $\mathbf{m_1}$ and $\mathbf{m_2}$. Potential energy of this interaction has the form:

$$U_{dd}(\vec{r}_{12}) = C\left[\frac{(\vec{m}_1 \cdot \vec{m}_2)}{r^3} - 3\frac{(\vec{m}_1 \cdot \vec{r}_{12})(\vec{m}_2 \cdot \vec{r}_{12})}{r^5}\right] \quad (1)$$

In the above equation, constant C is:

$$C = \frac{\mu_0}{4\pi} = 10^{-7}\left[\frac{H}{m}\right] \quad (2)$$

and the position vector connecting the two particles is $\mathbf{r_{12}} = \mathbf{r_1} - \mathbf{r_2}$. Distance between the particles is the moduo of this vector and we note it as r. Let us assume that magnetic moments belong to the same plane. In such a case, they have two components, one normal to the direction of $\mathbf{r_{12}}$, $\mathbf{m_n}$ and the other one parallel to it, $\mathbf{m_p}$. It leads to the expression for the potential energy:

$$U_{dd} = C\left[\frac{\left(m_{1n}m_{2n} + m_{1p}m_{2p}\right)}{r^3} - 3\frac{m_{1p}m_{2p}r^2}{r^5}\right] \quad (3)$$
$$\Rightarrow U_{dd} = C\frac{m_{1n}m_{2n} - 2m_{1p}m_{2p}}{r^3}$$

In the next figure, a sketch of the two dipoles that we are analyzing is shown.

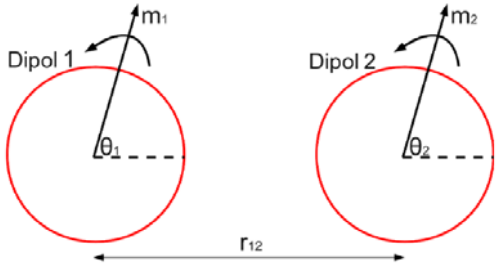

Figure 1. A sketch of two dipoles interacting via magnetic dipole-dipole interaction

Potential of their interaction has been derived. Let us normalize the values of the variables in it:

$$C = 1.\left|\vec{m}_1\right| = \left|\vec{m}_2\right| = 1, \vec{r}_1 = [000], \vec{r}_2 = [010] \quad (4)$$

Vectors $\mathbf{m_1}$ and $\mathbf{m_2}$ form the angles θ_1 and θ_2 with the direction of vector $\mathbf{r_{12}}$. Let us write:

$$m_p = m\cos\theta$$
$$m_n = m\sin\theta \quad (5)$$

There is a compact expression for the potential:

$$U_{dd} = C\frac{m_1m_2\sin\theta_1\sin\theta_2 - 2m_1m_2\cos\theta_1\cos\theta_2}{r^3} \quad (6)$$

Let us test how does the potential depend on the mutual orientation of the dipoles. We are scanning the angle θ_1 in 1000 points over the full range,, and angle θ_2 takes selected values. In Fig. 2 the potential depending on the mutual dipole orientation is shown. Potential has a minimum when the dipoles are parallel to vector $\mathbf{r_{12}}$ and they point to the same direction. It has a maximum when the dipoles have opposite directions, parallel to vector $\mathbf{r_{12}}$. The same stands if the dipoles are normal to vector $\mathbf{r_{12}}$, just the absolute values of the potential are smaller. Stars indicate the higher absolute value minimum and maximum, while triangles indicate lower absolute value minimum and maximum.

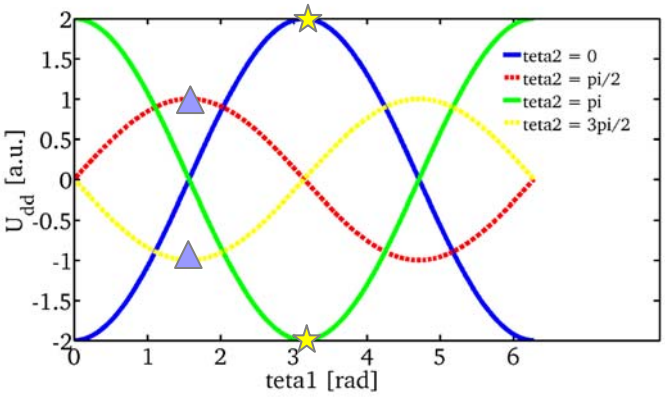

Figure 2. Potential of the dipole-dipole interaction depending on the dipole orientation

From the previous analysis, we have learned that two dipole orientations are of interest: parallel and normal to the vector $\mathbf{r_{12}}$. Distance was kept fixed and the dipole orientation was being changed. Now, we will keep the orientation fixed, but the distance will be changing.
In Fig. 3 a sketch of two dipoles parallel to the position vector $\mathbf{r_{12}}$ is shown. This system corresponds to the minimum marked with a star in Fig. 2.

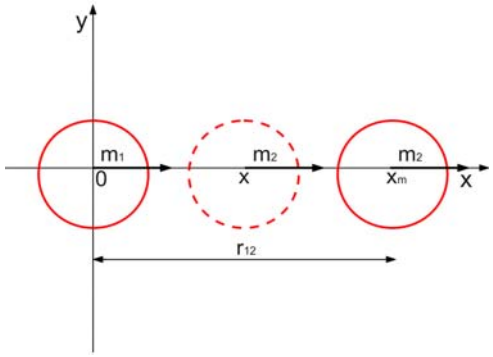

Figure 3. A sketch of two dipoles parallel to the position vector

In Fig. 4 dependence of potential on distance is shown. Obviously, absolute value of interaction potential decreases as the distance increases. This is an example of attraction between two dipoles. In Fig. 5 a sketch of two dipoles normal to the position vector $\mathbf{r_{12}}$ is shown. This system corresponds to the maximum marked with a triangle in Fig. 2.
In Fig. 6 dependence of potential on distance is shown. The same remark applies here, absolute value of interaction potential decreases as the distance increases. This is an example of repulsion between two dipoles.

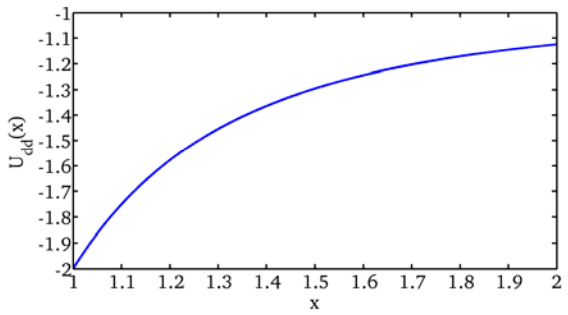

Figure 4. Dependence of the interacion potential on the position of dipole 2

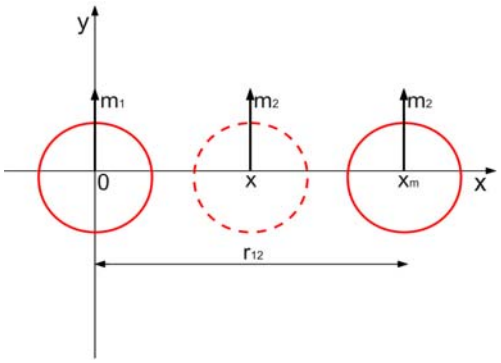

Figure 5. A sketch of two dipoles normal to the position vector

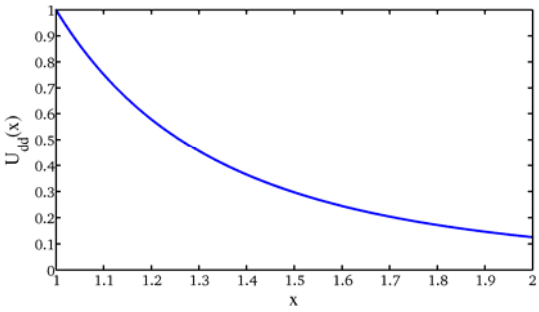

Figure 6. Dependence of the interaction potential on the position of dipole 2

This was the analysis of two systems of interest based on the general picture presented in Fig. 2. On the other side, from the Eq. 3, we can conclude that for a specific dipole orientation, interaction potential will be equal to zero [7]. We came up with a sketch shown in Fig. 7, in order to find out how does the system look like when this is the case. In Fig. 8 dependence of potential on distance is shown. When the angle is equal to the magic angle, potential is equal to zero. From the Eq. 3 we can derive what should be the angle α which causes the dipole-dipole interaction potential to be equal to zero.

$$\begin{aligned} & m_{1n}m_{2n} - 2m_{1p}m_{2p} = 0 \\ \Leftrightarrow\ & \sin^2\alpha - 2\cos^2\alpha = 0 \\ \Leftrightarrow\ & \alpha = \arccos\left(\frac{1}{\sqrt{3}}\right) = 54.74^\circ \end{aligned} \tag{7}$$

Angle α = 54.74° is the magic angle, interaction potential goes through the zero value at the x-coordinate (see Fig. 8) which corresponds to this angle. For this system, there is a switch of potential's sign, so there are both, attraction and repulsion between two dipoles.

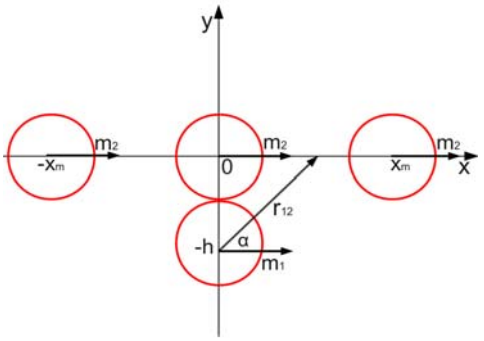

Figure 7. An illustration of the magic angle in the dipole-dipole interactions

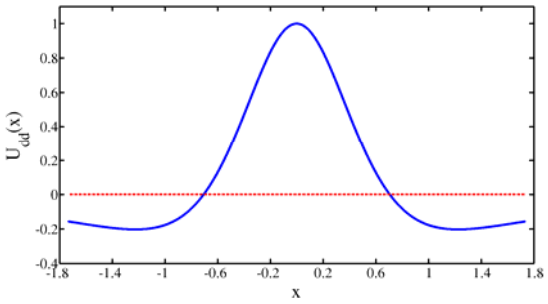

Figure 8. Dependence of the interaction potential on the position of dipole 2

III. CALCULATION OF THE BINDING ENERGY

In this chapter, a method for calculating the binding energy of a tubular structure is provided. Since we are analyzing infinitely long tubes, an efficient method for summing the dipole-dipole interactions of 1D periodical structures (periodical along one direction, the z-axis) had to be found. There are two well known and widely applied methods for this type of calculations, those are Ewald summs and Lekner method. Ewald sums are usually used for 2D periodical systems, while Lekner summation method converges faster in the 1D case, therefore we decided to implement Lekner method. The key feature of Lekner method is the choice of a periodic cell. It is a part of the infinite structure which is being replicated. Since we are dealing with tubes, one has to define its cell which is being replicated along the tube's axis (z – axis). Energy of an infinitely long tube is calculated as a sum of the self and cross energy. In next

expressions, we are dividing by N, since the energy is defined per particle, which allows a comparison of different structures with different number of particles in a cell.

Self energy represents the interaction energy of a selected particle in a cell, with all of its copies in the other cells. Total self energy is got as a sum over all particles in a cell, where number of particles in one cell is equal to N.

Self energy is given as [8]:

$$E_{self} = \frac{1}{L_z^3} \frac{\sum_{i=1}^{N} \left(1 - 3m_{z_i}^2\right) \zeta(3)}{N} \tag{8}$$

Cross energy represents the interaction energy of a selected particle in a cell, with all other particles of the same cell and with all their copies in the other cells. Total cross energy is got as a sum over all particles in a cell, i = {1, N}, j = {1, N} [8]:

$$E_{cross} = \frac{\sum_{i \neq j} U_{cross}\left(\vec{r}_i, \vec{r}_j, \vec{m}_i, \vec{m}_j, L_z\right)}{N} \tag{9}$$

In the above equation, the cross energy is got as a sum of cross potentials of pairs of particles (*i, j*). Cross potential is defined as a sum of four sums. In those sums a modified Bessel function of the second kind, zero and first order, K_0 and K_1 appears, respectively. In the following text, those sums are presented.

$$U_{cross}\left(\vec{r}_i, \vec{r}_j, \vec{m}_i, \vec{m}_j, L_z\right) = \sum_{i=1}^{4} S_i \tag{10}$$

Method for calculation of the binding energy of 1D infinitely long periodic structures is presented briefly. Goal of this paper is geometric formation and calculation of the binding energy of structures with minimal energy. Since the dipole orientation dictates the interaction potential, energy minimization means finding the optimal dipole orientation.

$$S_1 = \frac{-8\pi}{L_z^2}\left[\frac{2\left(\vec{m}_{\rho_i} \cdot \vec{\rho}\right)\left(\vec{m}_{\rho j} \cdot \vec{\rho}\right)}{\rho^3} - \frac{\vec{m}_{\rho_i} \cdot \vec{m}_{\rho j}}{\rho}\right] \times$$

$$\times \sum_{k=1}^{+\infty} k \cos\left(k\eta_z\right) K_1\left(k\eta_\rho\right)$$

$$S_2 = \frac{-16\pi^2}{L_z^3}\left[\frac{\left(\vec{m}_{\rho_i} \cdot \vec{\rho}\right)\left(\vec{m}_{\rho j} \cdot \vec{\rho}\right)}{\rho^2} - m_{z_i} m_{z_j}\right] \times$$

$$\times \sum_{k=1}^{+\infty} k^2 \cos\left(k\eta_z\right) K_0\left(k\eta_\rho\right)$$

$$S_3 = \frac{2}{L_z}\left[\frac{2\left(\vec{m}_{\rho_i} \cdot \vec{\rho}\right)\left(\vec{m}_{\rho j} \cdot \vec{\rho}\right)}{\rho^4} - \frac{\vec{m}_{\rho_i} \cdot \vec{m}_{\rho_j}}{\rho^2}\right]$$

$$S_4 = \frac{-16\pi^2}{L_z^3} \frac{\left(\vec{m}_{\rho_i} \cdot \vec{\rho}\right) m_{z_i} + \left(\vec{m}_{\rho j} \cdot \vec{\rho}\right) m_{z_j}}{\rho} \times$$

$$\times \sum_{k=1}^{k=+\infty} k^2 \sin\left(k\eta_z\right) K_1\left(k\eta_\rho\right) \tag{11}$$

IV. GEOMETRIC FORMATION OF THE STRUCTURES

In this paper we are analyzing tubes composed of magnetic particles. A specific configuration of a tube is defined by the geometry and the dipole orientation. There are two possible tube's geometries depending on the ring stacking. If the rings are stacked one on top of each other, those are AA tubes. Otherwise, if the rings are stacked in the way that there is one particle in the upper ring between two particles in the lower ring, those are AB tubes. There are only two ways of ring stacking, but there is a huge number of different dipole orientations. We took both stackings, and three well-defined dipole orientations. Those dipole orientations are called: single-thread (ST), multi-thread (MT) and ZZ dipole orientation. ST means that dipoles follow one thread that is tangential to the contour of the tube. MT means that dipoles follow multi threads of which the tube is composed, while ZZ means that all the dipoles are parallel to the z-axis. We have analyzed all three chosen dipole orientations for AA and AB tubes. When calculating binding energy of an infinite periodic structure using Lekner method, the key task is to define the periodic cell. In an AA tube, a cell is one ring. In an AB tube, a cell is composed of two rings. Normalization of the system includes dimension and energy scales. The diameter of every particle is d = 1. The distance between two particles is calculated from centre to centre, which means that the distance between two touching particles is equal to 1. On the other side, it is very convenient to introduce energy scale, so the energy is not defined in joules or electronvolts, but rather in arbitraty units [a. u.]. Energy scale is defined via repulsive potential of two touching dipoles standing side by side. The dipole moment is also normalized so that the length of dipole moment vector is equal to 1. Now we will explain geometric formation of the structures. For a tube, the basis is a ring composed of magnetic particles. In Fig. 9 the cross-section of a tube is presented.

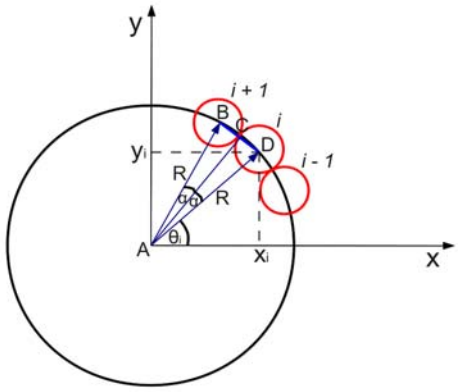

Figure 9. A sketch of the tube's cross-section

A ring is composed of N touching particles. Angular distance between two successive particles is $\Delta\theta = \frac{2\pi}{N}$ for an arbitraty chosen i-th particle, its angular position in respect to the positive x-semiaxis is $\theta_i = i\frac{2\pi}{N}$. Let us look at the triangle ABC in Fig. 9. Since the distance between touching particles is equal to 1, then BC = 1/2. There are relations:

$$\sin\alpha = \frac{1}{2R}$$
$$2\alpha = 2\frac{\pi}{N} \Rightarrow \alpha = \frac{\pi}{N} \tag{12}$$

Therefore, the relation between ring's radius and number of particles is:

$$R = \frac{1}{2\sin(\pi/N)} \tag{13}$$

A. Formation of AA tubes

In AA tubes, a periodic cell is one ring. Next array of equations defines coordinates of the particles, i = {1, N}.

$$x_i = \frac{1}{2\sin(\pi/N)}\cos\left(i\frac{2\pi}{N}\right)$$
$$y_i = \frac{1}{2\sin(\pi/N)}\sin\left(i\frac{2\pi}{N}\right) \tag{14}$$
$$z_i = 0$$

Dipole moments are defined in the next way, i = {1, N}.

$$\mu_{x_i} = \cos\left(i\frac{2\pi}{N} + \frac{\pi}{2}\right)$$
$$\mu_{y_i} = \sin\left(i\frac{2\pi}{N} + \frac{\pi}{2}\right) \tag{15}$$
$$\mu_{z_i} = 0$$

In the case of AA tubes, period along the z-axis is Lz = 1.

B. Formation of AB tubes

In AB tubes, periodic cell is a pair of rings. There are two arrays of equations, one for the lower ring, and another one for the upper ring. For the lower ring, coordinates of the particles are defined like in the case of AA tubes. There was a problem defining the z-coordinates of upper ring particles, which was solved using the definition of the distance between touching particles. Let us look at two arbitrary chosen particles in the lower ring (particles A and B) and one particle in the upper ring (particle C), which is placed between them. As it stands AC = BC = 1, from this condition we can derive how much are the upper ring particles displaced compared to the lower ring particles, along the z direction:

$$\Delta z = \sqrt{1-(x_A - x_C)^2 - (y_A - y_C)^2} \tag{16}$$

In the upper ring, coordinates of the particles are those:

$$x_i = \frac{1}{2\sin(\pi/N)}\cos\left(i\frac{2\pi}{N} + \frac{\pi}{N}\right)$$
$$y_i = \frac{1}{2\sin(\pi/N)}\sin\left(i\frac{2\pi}{N} + \frac{\pi}{N}\right) \tag{17}$$
$$z_i = \Delta z$$

In this case, period along the z-axis is Lz = 2 Δz.

V. Results of the Structure and Energy Calculations

In this chapter, results of the structure and energy calculations are presented. In Fig. 10, a geometry of one tube configuration is shown, obtained via MATLAB calculations. We are showing how does the tube (AA tube) look like in a side and in a top view.

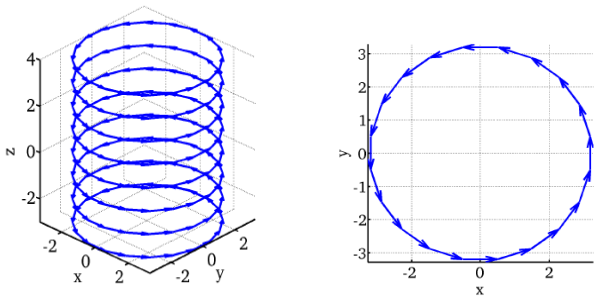

Figure 10. A side and a top view of an AA tube

In Fig. 11 and Fig. 12, dependence of binding energy on the confinement radius for AA and AB tubes is shown, including three different magnetizations.

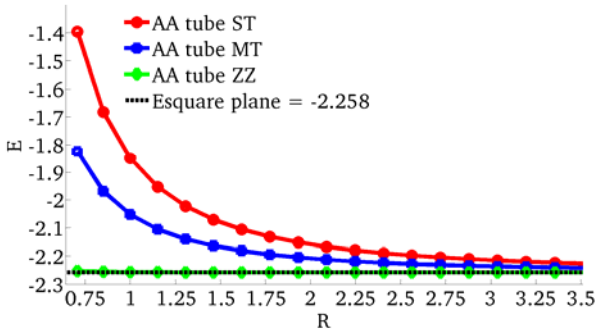

Figure 11. Energy in function of the confinement radius for different magnetizations (AA tube)

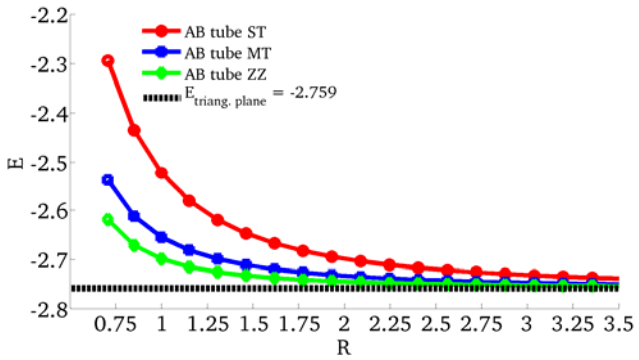

Figure 12. Energy in function of the confinement radius for different magnetizations (AB tube)

It is clear that for a fixed packing geometry (AA or AB), binding energy decreases as the magnetization changes from ST and MT into ZZ. Tubes with ZZ dipole orientation have minimal binding energy, and therefore they are the most stable tube configurations. When the confinement radius goes to the infinity, energy of all differently oriented tubes (ST/MT/ZZ) converges into the energy of an infinite plane. Energy of a square lattice plane is $E_{square} = -2.258$, all AA tubes converge into a square lattice plane. Energy of a triangular lattice plane is $E_{triangular} = -2.759$, all AB tubes converge into a triangular lattice plane.

VI. Conclusion

We have developed MATLAB simulations which form tubular structures composed of magnetic particles and calculate its binding energy. Both AA and AB ring stackings, including three different magnetizations, have been investigated.

From the results, we conclude that all those tube configurations are stable, since their binding energy is negative. For a fixed packing geometry (AA or AB), binding energy decreases as magnetization changes in the way:
ST - MT - ZZ. For a fixed magnetization, AB tubes have lower energy than AA tubes. Since AB tubes are more densely packed than AA tubes, we may say that bigger packing density implies lower binding energy and more stable structures.

Acknowledgement

I am thankful to dr Igor Stanković, my mentor from the Institute of physics at University of Belgrade, for the ideas, discussions and help in programming the simulations.

I am also thankful to my colleagues from the research group, for the help and support.

References

[1] G. M. Whitesides and B. Grzybowski, "Self-Assembly at All Scales", *Science*, Vol. 225, No. 29, 2002.

[2] D. J. Sellmayer, "Strong magnets by self-assembly", *Nature*, Vol. 420, No. 28, 2002.

[3] H. Zeng et al., *Nature*, Vol. 420, No. 395, 2002.

[4] M. Boncheva et al., *Proc. Natl. Acad. Sci*., USA 102, 3924, 2005.

[5] T. A. Prokopieva, V. A. Danilov, S. Kantorovich and C. Holm, "Ground state structures in ferofluid monolayers", *Phys. Rev. E, 80, 031404, 2009.*

[6] R. Messina, L. A. Khalil and I. Stankovic, "Self-assembly of magnetic balls: From chains to tubes", *Phys. Rev. E,* 89, 011202(R), 2014.

[7] L. Kocbach and S. Lubbad, "Geometrical simplification of the dipole-dipole interaction formula", *Physics Education*, Vol. 45, Issue 4, 2010.

[8] A. Grzybowski and A. Brodka, "Lekner type method for summing the dipole-dipole interactions", *Molecular Physics*, Vol 101, No. 8, 2003.

Tribology International (xxxx) xxxx–xxxx

Contents lists available at ScienceDirect

Tribology International

journal homepage: www.elsevier.com/locate/triboint

Molecular dynamics investigation of a model ionic liquid lubricant for automotive applications

Konstantinos Gkagkas[a,*], Veerapandian Ponnuchamy[b], Miljan Dašić[c], Igor Stanković[c]

[a] Advanced Technology Division, Toyota Motor Europe NV/SA, Technical Center, Hoge Wei 33B, 1930 Zaventem, Belgium
[b] Abylsen Belgium, 1000 Brussels, Belgium
[c] Scientific Computing Laboratory, Center for the Study of Complex Systems, Institute of Physics Belgrade, University of Belgrade, 11080 Belgrade, Serbia

ARTICLE INFO

Keywords:
Friction
Molecular dynamics
Ionic liquid
Drivetrain

ABSTRACT

In the current work we present a new modelling approach for simulating meso–scopic phenomena related to lubrication of the piston ring–cylinder liner contact. Our geometry allows a variable confinement gap and a varying amount of lubricant in the gap, while avoiding the squeeze-out of the lubricant into vacuum. We have implemented a coarse grain molecular dynamics description of an ionic liquid as a lubricant which can expand into lateral reservoirs. The results have revealed two regimes of lubrication, an elasto-hydrodynamic one under low loads and one with low, velocity-independent specific friction, under high loads. The observed steep rise of normal forces at small plate-to-plate distances is an interesting behaviour that could potentially be exploited for preventing solid–solid contact and wear.

1. Introduction

Friction accounts approximately for one-third of the fuel energy consumed in passenger cars [1], therefore a deeper understanding of the lubrication mechanisms in engineering systems is necessary. Atomic-scale simulations can provide important insights which are necessary for understanding the underlying mechanisms that can affect the system behaviour, such as structural changes in lubrication layers during shear as well as the interaction between lubricants and surfaces. The field of computational lubricated nanotribology has been well established over the last decades [2,3] and the availability of increased computational resources is allowing the application of such methods in cases with increasing complexity. Recent studies of nanoscopic friction based on Molecular Dynamics (MD) include, for example, the study of fatty acids [4] and ionic liquids ILs [5] as lubricants. Wear reduction demands and the drive to keep friction low, have led to reduced lubricant film thickness down to only a few molecular layers [6–9]. MD can enable us to access and understand the behaviour of very thin films which are subjected to compression and shearing between walls [6–8].

Our specific goal is to achieve a representation of the tribological system which is relevant to automotive powertrain applications. As approximately 45% of the engine friction losses occur in the piston assembly [1], our initial target is to mimic the conditions observed in the piston ring–cylinder liner contact, in terms of pressure, temperature and shear rates. In addition, in order to be able to achieve length– and time–scales that can be of relevance to the real–life systems, it is necessary to apply appropriate simulation methodologies, such as the use of coarse grain molecular dynamics [10–13].

In recent years, the application of ILs as advanced lubricants is being studied with a steadily increasing interest [14]. The use of ILs as both neat lubricants and additives for engine lubrication has been considered [15–17]. Significant improvements on friction and wear reduction have been observed experimentally [16], rendering this concept of potential interest to industry. However, unravelling the mechanism of nanoscopic friction in ILs together with their structure poses a great scientific challenge, and so far few studies in this direction have been performed, e.g., Ref. [18]. ILs are molten salts typically consisting of large-size organic anions and cations. Physical properties of ILs, such as negligible vapour pressure, high temperature stability (they do not evaporate or decompose at temperatures of interest for automotive industry) and high ionic conductivity render them potentially relevant to lubrication. In addition, their properties can be modified by an applied voltage using confining surfaces which are charged in order to build up an electric field across the nanoscale film. The applied potential can affect the structure of IL layers and lead to externally controllable lubricating properties [18,19]. There is also significant flexibility in tuning the physical and chemical properties of ILs which can affect lubrication such as viscosity, polarity and surface reactivity by varying their atomic composition as well as the anion–cation combination. An important observation is that ILs confined

* Corresponding author.
E-mail address: Konstantinos.Gkagkas@toyota-europe.com (K. Gkagkas).

http://dx.doi.org/10.1016/j.triboint.2016.12.017
Received 20 July 2016; Received in revised form 5 December 2016; Accepted 12 December 2016

between surfaces feature alternating positive and negative ionic layers, with an interlayer separation corresponding to the ion pair size [20,21].

Previous work employing Lennard-Jones fluids has provided insights on the complete dynamic diagram of confined liquids including wall slip, shear banding, solid friction, and plug flow. In terms of fluid complexity these studies have mainly employed mono-atomic systems, and only a few authors have considered mixtures of molecules [22,23]. In addition to inherently being a mixture of cation and anion molecules, ILs involve long range Coulomb interactions inducing long range order on far greater scales than the IL itself [5,9,24]. Detailed investigation of ILs as lubricants at the nanoscale is therefore essential for exploring the potential of implementing them in lubrication systems.

In this study, we apply a coarse-grained model for the description of nanoscopic friction mediated by a liquid lubricant because based on recent studies [18,19,21] it was shown that if the molecules interact via non-bonded potentials (Lennard-Jones and Coulombic), this can capture all main physical attributes of the IL-lubricated nanotribological system.

This paper is organised as follows: Section 2 introduces the MD setup of the solids and lubricants used, while the motivation for the choices made is provided. In Section 3, the structural properties of the modelled IL under bulk and confined conditions are discussed. The results stemming from the friction MD simulations are then presented in Section 4 followed by some concluding remarks in Section 5.

2. Model

Under typical operation of internal combustion engines, the conditions inside the combustion chamber vary significantly. Temperature can range from 300 K to values higher than 2000 K, while pressure ranges from atmospheric to values higher than 10 MPa [1]. The piston reciprocates with a sinusoidal velocity variation with speeds varying from zero to over 20 m/s. The time required for one revolution of the engine is of the order of 10 ms, while the total distance travelled by the piston over this period is of the order of 0.2 m. Such scales are typically modelled using continuum mechanics simulations. However such simulations cannot provide the physical insight which is necessary for understanding the molecule–dependent processes that affect the tribological phenomena. For this purpose, we have developed a coarse grain MD configuration that can provide useful insights to molecular processes, while remaining relevant to conditions observed in real–life systems. More specifically, in this section we will describe a setup of MD simulations developed with the aim of building a framework that incorporates meso–scale features of the piston ring–cylinder liner system and permits an efficient implementation of different solid surfaces and lubricants.

2.1. Geometry

All MD simulations in this study were performed using the LAMMPS software [25]. The geometry used in our friction simulations is shown as a schematic in Fig. 1, along with the dimensions of our system as well as the number of the MD particles used. The simulation setup was loosely inspired by previously published research by others [5,18,19,21]. By implementing such a geometry we have attempted to achieve: (i) a realistic particle squeeze–out behaviour with the formation of two lateral lubricant regions (in a similar manner to the simulations of Capozza et al. [21]) and (ii) a system that allows the lubricant to be externally pressurised. For the description of the solid surfaces we have combined rigid layers of particles moving as a single entity on which the external force or motion is imposed, denoted by “Top Action” and “Bottom Action” in Fig. 1(A), with thermalised layers (denoted by “Top Thermo” and “Bottom Thermo”) in which particles vibrate thermally at T=330 K. The Nose-Hoover NVT thermostat is used to control the temperature. As in previous MD simulations [9,18,19,21,24], under similar operating conditions, the details of the adopted dissipation scheme are not expected to change the essence of the system response on mechanical deformation. The relaxation time of the Nose-Hoover NVT thermostat for the lubricant and the solids is 200 fs (cf. Ref. [9]). The plates were treated as rigid bodies, with the lower one being fixed and the upper one subjected to a z-directed force F_z (the load) as shown in Fig. 1(A) and driven along x direction at a constant velocity. The solid plates were made up of densely packed atomic layers at a FCC (111) lattice arrangement. Periodic boundary conditions were applied in the x and y directions. The bottom plate can therefore be considered to be infinite, while the top plate is surrounded by vacuum pockets on its sides, so called lateral reservoirs, in which the lubricant can freely expand. The lateral reservoirs were implemented as a mechanistic way for allowing the lubricant to be dynamically squeezed in or out as an external load or velocity is applied, or due to local fluctuations during the simulation progression. At the same time, the lubricant remains an infinite continuous body in x and y directions, similar to the conditions observed in a real tribological system from a meso–scopic point of view. This is especially important if the system experiences partial or complete crystallisation under compression, cf. Section 4 and Fig. 8.

While the total number of considered lubricant molecules is constant, the finite upper plate width and the resulting free space enables the particles to be squeezed-out even to the extent where due to structural changes the lubricant ceases wetting the solid plates. The number of lubricant molecules effectively confined inside the gap can therefore dynamically change depending on the loading conditions. This is important for exploring the possible states of a mechanical system of particles that is being maintained in thermodynamic equilibrium (thermal and chemical) with a lubricant reservoir (i.e., void spaces in tribological system). The nano-tribological system is open in the sense that it can exchange energy and particles, realising an effectively grand-canonical situation, cf. Fig. 1(b) and Ref. [26].

2.2. Solids and lubricant model

By using our simulation setup, we aim to study the lubrication properties of several lubricants. As a first step, in the current study we have implemented an ionic liquid as a lubricant. On the atomic level ILs are usually made up of large-size irregular organic anions and cations often including long alkyl chains. In the current work we have applied a simple coarse-grained model for its description, consisting of a charged Lennard-Jones system where anions and cations have different radii as already exploited in previous studies in the literature [21]. According to that, we have implemented a Lennard-Jones (LJ) 12-6 potential combined with a Coulombic electrostatic potential:

$$V(r_{ij}) = 4\epsilon_{ij}\left[\left(\frac{\sigma_{ij}}{r_{ij}}\right)^{12} - \left(\frac{\sigma_{ij}}{r_{ij}}\right)^{6}\right] + \frac{1}{4\pi\epsilon_0\epsilon_r}\frac{q_i q_j}{r_{ij}} \quad (1)$$

Parameters $\{\epsilon_{ij}, \sigma_{ij}\}$ define the LJ potential between different types of particles i, j = A, C, P which refer to anions, cations and solid plate atoms, respectively. The numerical values for each pair are listed in Table 1. The diameter of cations was set to σ_{CC} = 5 Å and anions to σ_{AA} = 10 Å, in order to explore the effect of asymmetry of ion sizes (similar to Ref. [21]). Atoms of the solid plates have a diameter of σ_{PP} = 3 Å. The plates consist of nine densely packed layers in a FCC (111) lattice.

The ions were modelled as coarse grain particles, the charge of which was set to elementary: $q_A = -e$ and $q_C = +e$, i.e., $e = 1.6 \times 10^{-19}$ C. The ionic liquid is neutral, so the total number of cations and anions is the same: $N_C = N_A = N_{IL}/2$. In the present simulations, the number of ions used was N_{IL} = 2500. The dielectric constant was set to $\epsilon_r = 2$ to account for the dielectric screening, as in Refs. [19] and [21]. The LJ potential has a short-range impact, since it vanishes rapidly as the distance increases $\propto r^{-6}$, while the Coulombic

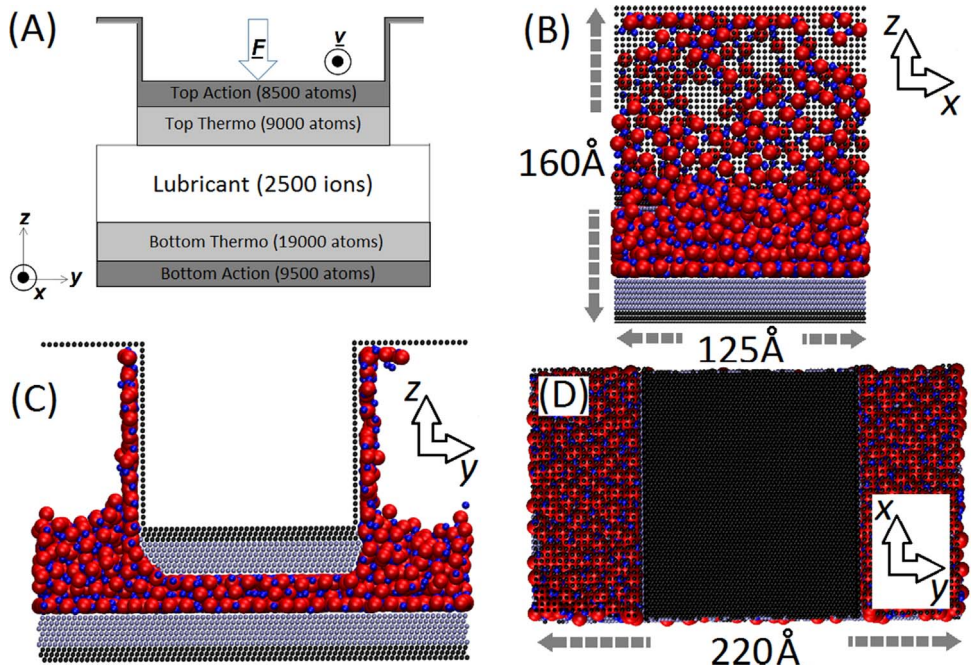

Fig. 1. (A) Schematic of the simulation setup shown as yz cross-section. There are two solid plates at the top and bottom of the system, consisting of two regions: at the outermost ones the particles are moving as a single entity (Top/Bottom Action) and at the innermost ones the particles are at a controlled temperature (Top/Bottom Thermo). The thermalised layers are in direct contact with the lubricant while the action layers are used to impose external velocity and/or force to the solid plates. (B)–(D) Side views of the typical simulation configuration and key dimensions of the geometry. (B) Side (*xz*) view with respect to the shear direction. (C) Front (*yz*) view in the direction of the top plate motion. (D) Top (*xy*) view of the system. The solid plates are made up of FCC (111) atomic layers. The ionic liquid is composed of an equal number of cations (blue spheres) and anions (red spheres). (For interpretation of the references to color in this figure legend, the reader is referred to the web version of this article.)

Table 1
List of LJ parameters used in simulations.

Pair ij	ϵ_{ij} [kCal/mol]	σ_{ij} [Å]
CC	0.03	5
AA	0.03	10
CA	0.03	7.5
PC	0.3	4
PA	0.3	6.5
PP	120	3

potential has a long-range impact, $\propto 1/r$. To handle long–range interactions, we have used a multi-level summation method (MSM) [27], since it scales well with the number of ions and allows the use of mixed periodic and non-periodic boundaries that are featured in our setup. To sum up, IL ions and plate atoms interact with each other via LJ potentials. In addition a Coulombic electrostatic potential is added in ion-ion interactions.

In engineering applications, the lubricant molecules typically interact with metal surfaces. Computationally efficient many–body potentials such as embedded atom method (EAM) potential [28,29] can be applied for the description of such solids. Such schemes have been employed extensively for modelling a wide range of systems including metals [29] and metal-metal oxide interfaces [30]. In addition, in order to account for the induced charges on the metallic conductor surface by the ions, the Drude-rod model developed by Iori and Corni [31] which consists of the addition of an embedded dipole into each metal atom, thus rendering it polarisable, has been applied in previous studies [5]. Since in our initial stage of IL tribological behaviour research, modelling the elasticity of metallic plates plays a secondary role, we have selected a simplified model in which plate atoms interact strongly with each other if they belong to the same plate, i.e., $\epsilon_{PP} = 120$ kCal/mol, as opposed, to a very weak interaction between the different plates $\epsilon_{top/bottom} = 0.03$ kCal/mol. Furthermore, even though the typical engineering systems are often metallic, our initial coarse grain MD study of liquid dynamics according to the applied conditions justified the implementation of a simpler solid system which does not feature substrate polarisation. Finally, it is possible that the actual surfaces might feature carbon coatings or depositions, in which case the surface polarisation can be of secondary importance.

The starting configuration for our MD simulations was obtained via a relaxation process. In order to obtain a stable and reproducible initial configuration, the relaxation was performed through a stepwise increase of absolute ion charge at steps of $\Delta|q_i| = e/10$, i=A, C. Each time the charge of the ions was increased, a minimisation of the system's energy through conjugated gradient method was performed. In this way, the system characteristics were gradually converted from pure LJ to a Coulomb interaction dominated system through a series of stable configurations.

As we are aiming at understanding the lubricant behaviour at mesoscopic conditions observed in a ring–liner system, we have attempted to include in our MD model the potential IL pressurisation that can occur due to the liquid flow resistance, as well as the variable pressure arising from the reacting gas in the combustion chamber. Inserting gas molecules directly in the simulation for this purpose would require a reduction of the time step due to higher thermal velocities of the gas. In turn, the computational cost would increase significantly making simulations impossible to run in realistic computational time. Therefore, in order to understand the effect of external pressure on the IL behaviour, we have applied a repulsive force between the topmost rigid solid layer and the IL particles in the form of a truncated and shifted LJ potential. Two cases with cut-off distances at 15 Å and 4 Å above the outermost top plate layer were studied so that the IL inside the confinement gap would remain outside the influence zone of this mechanistic force. By appropriate selection of the LJ parameters for this potential, the resulting external pressures applied on the unconfined surface of the IL were 120 kPa and 250 kPa, respectively.

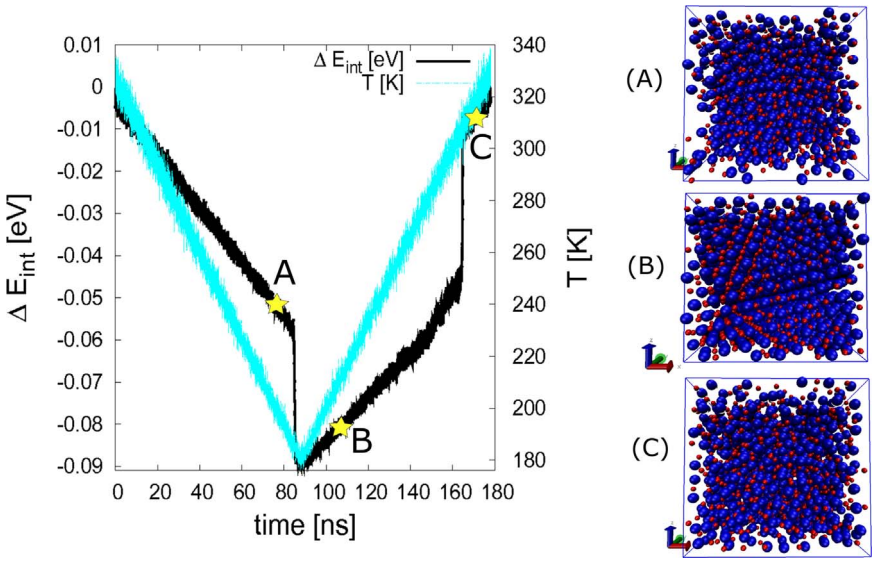

Fig. 2. (Left): Bulk internal energy change and temperature of the ionic liquid as a function of simulation time. (Right) Snapshots of ion arrangement at liquid (A), (C) and solid (B) state.

3. Probing ionic liquid's internal structure behaviour

3.1. Solidification and melting of bulk ionic liquid

In order to confirm that the IL used in our MD simulations remains in a liquid state for the conditions of interest, its liquid–solid and solid–liquid phase transitions were initially studied. A bulk IL configuration was prepared by placing the same number of cations and anions $N_c = N_a = 1000$ into a 3D periodic box, with pressure kept constant at 100 kPa. Phase transitions were then achieved via the application of linear ramping to the temperature, in a similar approach to the calculations performed in Ref. [21].

Starting from an initial temperature $T_1 = 330$ K where the IL is in liquid state, the temperature was decreased linearly down to $T_2 = 180$ K. The absolute rate of temperature change was: $|dT|/dt = 1.67$ K ns^{-1}. A liquid–solid phase transition was observed during the IL cooling. After reaching $T_2 = 180$ K, the temperature was increased back to the initial value of 330 K. This heating process caused with its turn a solid–liquid phase transition. In Fig. 2 the IL internal energy change ΔE_{int} and temperature T are shown as functions of time t. The temperature profile follows the applied conditions and its superimposition to internal energy change allows the observation of the dynamic behaviour of the liquid. By plotting the averaged internal energy change of the IL against its temperature in Fig. 3, the hysteresis behaviour in the solidification–melting cycle is clearly observed, while the phase transition locations can be clearly defined. It can be seen that during the cooling process, the internal energy of IL linearly decreases until the temperature reaches $T_{ls} = 190$ K, at which point a sharp drop is observed. This indicates a first order thermal phase transition (liquid–solid). During the heating process, a similar sharp jump of energy is observed at $T_{sl} = 305$ K which corresponds to an opposite phase transition (solid–liquid). The obtained results are in a good agreement with Ref. [21] and confirm that the IL is behaving as a liquid for temperatures higher than 310 K, under atmospheric pressure conditions. In the rest of our calculations a temperature value of T=330 K was applied, in order to allow a liquid state that is combined with local solidification under elevated contact pressure conditions.

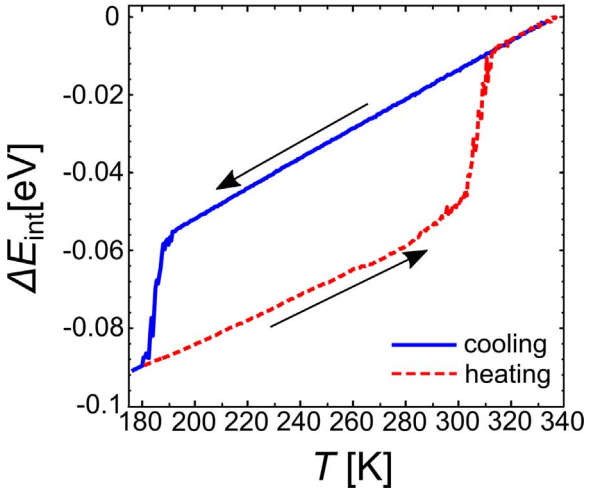

Fig. 3. Bulk internal energy change of the ionic liquid as a function of temperature. The internal energy was calculated by averaging on segments of $\Delta T = 0.5$ K.

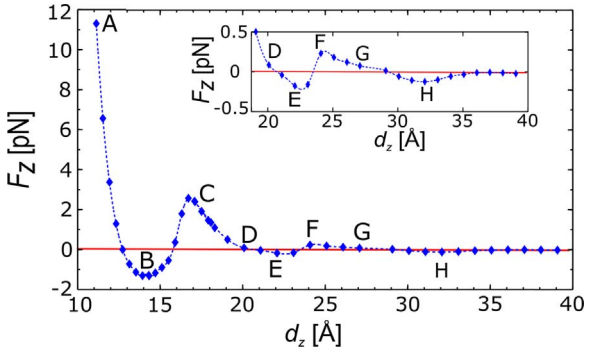

Fig. 4. Dependence of normal force F_z on plate-to-plate distance d_z. Eight characteristic points $\{A, B, C, D, E, F, G, H\}$ with corresponding interplate distances $d_z = \{11, 14, 17, 20, 22, 24, 27, 32\}$ Å are marked on the $F_z(d_z)$ curve. The horizontal solid line denotes F_z=0 pN. The dashed line connects the points obtained from the simulation and serves as a visual guide.

3.2. Ionic liquid structure in thin film

The confinement has a profound influence on the structure of ILs in thin films [20,26,32]. The confining surfaces can induce ordering of the particles in their vicinity. The resulting structure and forces are a result of the interplay between the limited volume and the particles which fill the space. In Fig. 4, the force-distance characteristic of our system is

presented. The solid horizontal line denotes the zero normal force level (i.e., F_z=0). A non-monotonous behaviour of the normal force F_z acting on the top plate can be observed as the plate-to-plate distance is changing. This distance corresponds to the gap between the plates where the IL is under confinement. The points (d_z, F_z) were obtained through our simulations, while the dashed line serves as a visual guide. It can be seen that the normal force strongly depends on the inter–plate distance and that it also becomes negative in certain regions. This can be translated as the IL striving to reduce the plate-to-plate distance due to adhesion phenomena. These changes of the normal force are correlated with the extraction and inclusion of IL layers into the gap, as already observed experimentally, cf. Ref. [20]. During the performed simulations, the cationic-anionic layers were squeezed out in pairs, in order to keep the system locally neutral, as observed in experimental studies [20,26,32–34].

Concerning the realisation of the simulations presented in Fig. 4, the inter–plate gap was modified in the following manner: the top plate was displaced towards the bottom one with a constant velocity v_z=5 m/s. For $d_z < 17$ Å the velocity was reduced to v_z=1 m/s. At each calculation point shown in Fig. 4, the top plate was kept fixed for a period of time t_{static} = 50 ps, during which period the average value of the normal force was calculated. The process was repeated until a distance $d_{z,min}$ = 11 Å was reached.

In order to understand the dynamic evolution of our system, snapshots of the system from the MD simulations corresponding to several characteristic points in the $F_z(d_z)$ curve were selected and studied in more detail. Fig. 5 shows the configuration and ion density distribution along the z–direction for eight characteristic points {A, B, C, D, E, F, G, H}, corresponding to plate-to-plate distances d_z = {11, 14, 17, 20, 22, 24, 27, 32} Å respectively. The ions are deliberately depicted smaller than their LJ radii in order to allow a direct observation of the layering. The position of the atomic centres of the innermost atomic layers of the top and bottom plate are indicated in Fig. 5 as z_T and z_B respectively. As the bottom plate was fixed, z_B remains constant while z_T changes with the top plate displacement.

A general feature observed under all conditions was the fact that the cations always formed the layer closest to the bottom plate. The reason is the smaller size of the cations (σ_{CC} = 5 Å) compared to the anion species (σ_{AA} = 10 Å). Following this, a second layer was induced by the first one and populated only by anions. The distance between the first and the second layer from the bottom is in the range of 1 – 2.5 Å, meaning that while the centres of mass of the particles are in different layers, the layers themselves overlap as their distance is smaller than the particle diameters. In the rest of this section, the changes in the number of layers as the inter–plate gap is reduced will be presented and correlated with the changes in the normal force F_z which is acting on the top plate.

For the minimum simulated plate-to-plate distance d_z=11 Å, shown in Fig. 5(A) we can observe a pronounced peak in the anion density distribution close to the bottom plate which is aligned with a well-defined anionic layer inside the gap. The anion peak is marked with the “1CU” annotation. In the case of cations, there are two peaks attached below and above the anionic peak. This situation corresponds to the formation of two incomplete cationic layers inside the gap. With increasing plate-to-plate distance d_z the normal force F_z is decreasing, with a sign change of F_z at d_z=12.7 Å. In the range 12.7 Å < d_z < 15.7 Å the normal force remains negative. This means that the IL is pulling the plates together, since the ions strive to reduce their interlayer distance, as well as the distance between themselves and the plate atoms. Such behaviour is typically observed in systems exhibiting layering transition, already seen in systems of both neutral molecules [2] and ILs [20]. With further increase of d_z the force becomes positive again, and reaches a local maximum at the point (C) in Fig. 4. At this point we observe a change in the number of anion layers confined in the gap from one to two, as shown in Fig. 5(C).

In Fig. 5(C), the plate-to-plate distance is d_z=17 Å and the two bottom peaks of the anion/cation density distribution, denoted by “1CU” and “2C”, are inside the gap. A third smaller anion/cation density peak, denoted by “2U” in Fig. 5(C), is the result of the ordering initiated at the bottom plate's surface and is actually outside the confinement gap. The vertical distance between the peaks “2C” and “2U” is approximately 3.5 Å and corresponds to the effect of the compression of the IL from the top plate. Further increase of the plate-to-plate distance results in a continuous decrease of the normal force without a sign change as the positions of peaks “2C” and “2U” become aligned, cf. Fig. 5(D) for a distance d_z=20 Å. Further increase of the inter–plate distance results once more in a reversal of the sign of the normal force (i.e., $F_z < 0$ for 21 Å < d_z < 23.5 Å). At the mid point between the plates a broad maximum of cation density distribution can then be observed, see Fig. 5(E). The cations, as smaller particles, have a tendency to fill the space between the more stable anionic layers. When the anions also start to form a third layer at the midpoint between the two plates the corresponding cationic peak of density becomes sharper and the normal force becomes positive again, see Fig. 5(F). In this case the cations can form a layer more easily while the anions remain scattered. This is the opposite behaviour to the one typically observed, where the larger anions tend to order more strongly due to the excluded volume effect [35]. From Fig. 5(F) to Fig. 5(G) an interesting transition can be observed, during which the single well resolved cation peak disappears and a less pronounced cation–anion pair peak takes its place. Finally in Fig. 5(H) at d_z=32 Å, we observe the clear formation of three anion and four cation peaks.

Considering engineering applications, the steep rise of the normal force at small plate-to-plate distances, i.e., $d_z < 14$ Å can be beneficial for protecting against solid-solid contact and consequent wear. On the other hand, there is also a strongly decreasing trend of maximal normal force which can be sustained by the system as the number of ion layers confined between the plates increases, i.e., for two cation layers the maximal force $F_{z,max}$ = 3 pN, while for three it is $F_{z,max}$ = 0.25 pN. In our model, the Lennard-Jones interaction between the plates and the ions is ten times stronger than between the ions themselves. The ion layers closest to the plates are therefore more stable than the layers in the midpoint of the gap (see Fig. 5(F)). As a result, the three layer system becomes less dense, and can build up a lower normal force compared to the two layer system (in Fig. 5(C)).

4. Friction simulations

Following the detailed study of the static system, we turn our focus to dynamic conditions, where there is a relative motion between the plates in x direction and as a result frictional forces can be observed. The dynamics of the plates impact the IL and result in an overall longitudinal force acting on each solid body. In order to evaluate the trends of specific friction we have performed simulations at different plate velocities and at two interplate distances. The simulations have been performed for a broad range of top plate velocities v_x = 0.1, 0.2, 0.5, 1, 2, 5, and 10 m/s, with the bottom plate kept fixed. We have compared cases with different external pressures applied on the IL p_{ext} = 0, 120 and 250 kPa and two distinct plate distances d_z=17 and 27 Å. The simulations were performed as follows: Points (C) and (G) in Fig. 5 were chosen as the starting configurations. The simulations ran until the top plate had covered a distance of d_x=50 Å in x direction. Therefore cases with lower velocities required increased total time. The forces acting on the top plate were monitored, as shown in Fig. 6 for a randomly chosen case. It was observed that the normal force remained roughly the same after the onset of the simulation. Steady–state conditions were assumed following a displacement of d_x=10 Å, and then average values were calculated using the statistics until the completion of the simulation.

The results for the specific friction are shown as a function of sliding velocity in Fig. 7. The specific friction $\langle F_x \rangle / \langle F_z \rangle$ is defined as the ratio of

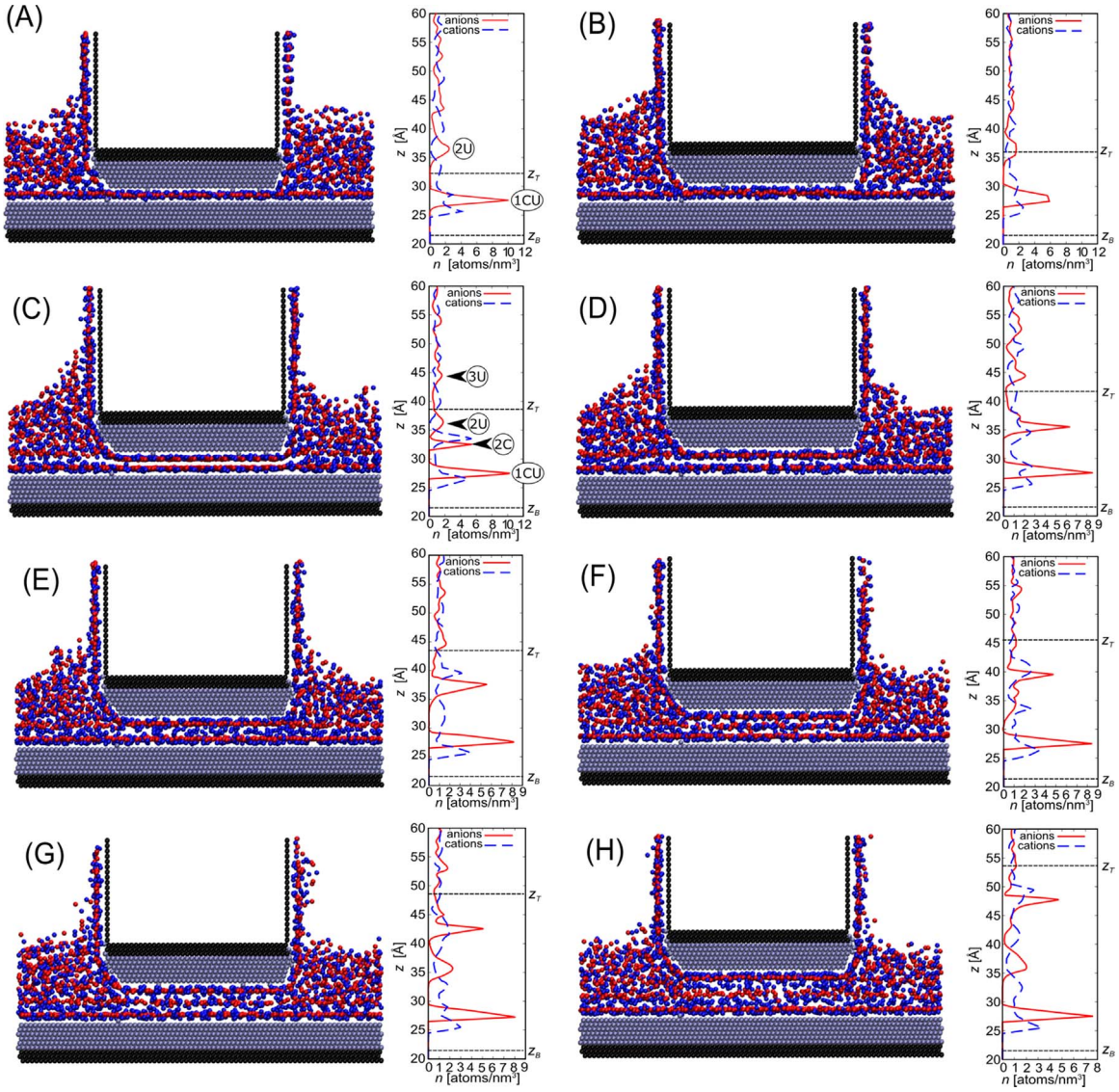

Fig. 5. Snapshots of system configurations at points {*A*, *B*, *C*, *D*, *E*, *F*, *G*, *H*} from Fig. 4 and corresponding density distribution of anions/cations along the *z*-axis. The position of the atomic centres of the innermost layer of the top and bottom plate is denoted by z_T and z_B, respectively. The bottom plate is fixed and $z_B = 21$ Å. The ions are deliberately depicted smaller than their LJ radii in order to allow a direct observation of the layering. In Figures (A) and (C) the annotations indicate the anion layer vertical order from the bottom (1, 2, 3) and the lateral placement: (C)onfined and (U)nconfined.

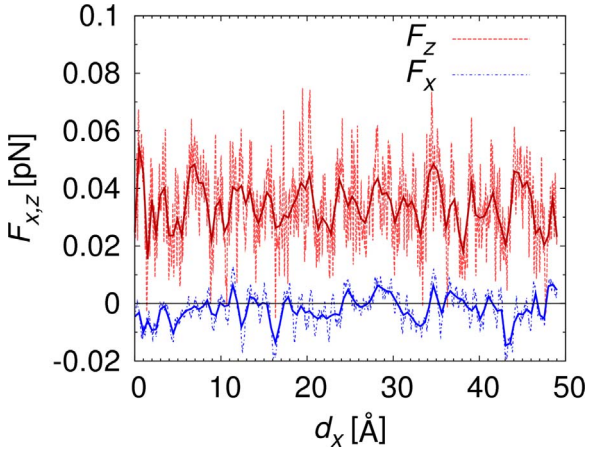

Fig. 6. Temporal evolution of total normal and axial forces acting on sliding surface for plate-to-plate distance d_z=27 Å and top plate axial velocity v_x=10 m/s. Dashed lines show the raw numerical data which are smoothed using the solid lines for a clearer identification of temporal trends.

the time averaged frictional and normal force F_x and F_z respectively and is different to the Coulomb friction coefficient $\mu = \partial F_x/\partial F_z$. In our simulated cases we have observed either a weak or a logarithmic dependence of specific friction on velocity. The numerical values were fitted to a linear function of the form $\langle F_x\rangle/\langle F_z\rangle = a\log(v_x/v_{\text{ref}}) + b$, where $v_{\text{ref}} = 1$ m/s. The coefficients a, b obtained from the simulation data are listed in Table 2. A reasonable fit to the linear regression curve can be observed for most cases. In the case of $p_{\text{ext}} = 120$ kPa, the system is potentially in a transition between the two significantly different cases of zero and high pressure, which can explain the poorer quality of the fit to the linear curve. The logarithmic dependence indicates typical elasto-hydrodynamic lubrication conditions [36]. On the other hand, the weak dependence of specific friction on velocity has also been observed in previous studies of IL lubrication, cf. Refs. [5,24].

4.1. Impact of ionic liquid confinement gap

The influence of plate-to-plate distance on specific friction was initially analysed, while the applied external pressure on the IL p_{ext} was kept equal to zero. In contrast to previous studies of IL lubrication

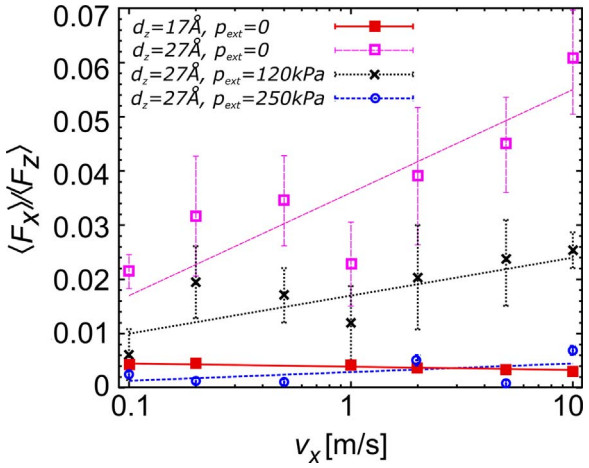

Fig. 7. Dependence of specific friction $\langle F_x\rangle/\langle F_z\rangle$ on velocity at external pressures p_{ext} = 0, 120 and 250 kPa and inter-plate distances d_z=17 and 27 Å. The error bars represent the standard deviation of the average values obtained from the simulation data. The curves showing the specific friction trends were obtained by linear regression and the corresponding parameters are listed in Table 2.

Table 2
Results for the coefficients a, b in the relation $\langle F_x\rangle/\langle F_z\rangle = a\log(v_x/v_{ref}) + b$, where v_{ref} = 1 m/s. The results were obtained using the least-squares method.

Case	a	b	R^2
(A) d_z=17 Å, p_{ext} = 0 kPa	−0.0006(2)	0.0039(2)	0.63
(B) d_z=27 Å, p_{ext} = 0 kPa	0.016(5)	0.036(3)	0.72
(C) d_z=27 Å, p_{ext} = 120 kPa	0.007(2)	0.017(2)	0.26
(D) d_z=27 Å, p_{ext} = 250 kPa	0.002(1)	0.003(1)	0.62

[5,24], our system showed a strong crystalline order induced by confinement. The normal force was roughly ten times higher in the case of the smaller plate-to-plate distance, i.e., for d_z=17 Å compared to d_z=27 Å. On the other hand, the lateral force F_x remained at similar levels, therefore leading to a sharp decrease of the specific friction values. At the same time, the weaker confinement and the smaller normal force for d_z=27 Å resulted in a steeper slope of the curve $\langle F_x\rangle/\langle F_z\rangle$.

In order to understand the potential correlation of the IL structure with the arising frictional forces, the confinement zone was observed in detail using Fig. 8, where a side view (left side) and top view (right side) of the system is shown. In the top view, the system is shown with the solid and IL particles above the upper plate plane removed. In this plot the ions are depicted with their corresponding LJ radii in order to achieve a realistic visualisation of the structure. The anions form a locally cubic structure, cf. right panel Fig. 8(A), while the crystal direction of the cubic structure is indicated with dashed lines. If we look into the structure of the IL in the confinement zone, Fig. 8(A) and (B), we can observe a single, well resolved crystal structure in the case of d_z=17 Å, while in the case of d_z=27 Å some defects are present. It can also be observed that outside the gap, the IL remains in a disordered, liquid state.

Further clarification can be attained by plotting the ion density distribution profiles inside and outside the gap in Figs. 9(A) and (B). It can be observed that at the plate-to-plate distance d_z=17 Å, both cation and anion peaks of density distribution function inside the gap are narrow and sharp. In addition, both the anion and cation peaks in each paired layer are located at approximately the same z location. These findings confirm that under these conditions the IL is in a crystalline, “solid-like” state with minimum disorder. In the case of a wider gap d_z=27 Å the anion peaks next to the walls remain narrow, with a third broader one appearing in the centre. The cation arrangement is more dispersed, with double peaks appearing above and below each anion

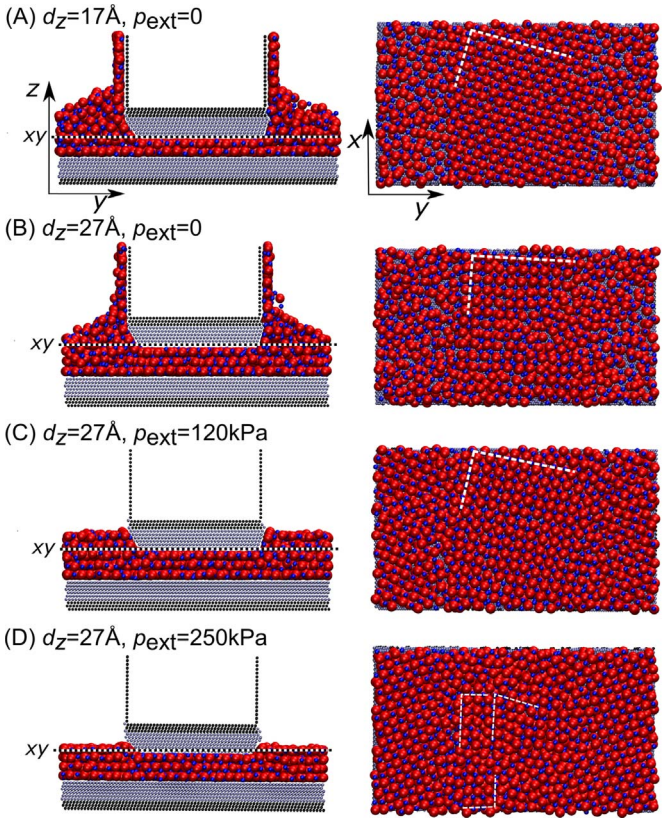

Fig. 8. Side (yz) and top (xy) views of snapshots from four separate friction simulations. The top views correspond to the planes marked with dashed lines in the side views and do not include the solid and IL particles above the upper plate plane. The ions are depicted according to their LJ radii in order to visualise the crystalline structures. The dashed lines in the top views denote the crystal direction of self-formed cubic structures.

peak. These statistics indicate a more layered, less strictly ordered state. The difference in the extent of confinement induced crystallisation is a probable reason for the observed steep slope of specific friction since the observed defects can interact more strongly with the upper plate at higher velocities and contribute to the increase of friction force. Our observations show some similarity to the behaviour previously seen in Lennard-Jones systems where systems at pressures above a certain critical value and at sufficiently low velocities exhibited such behaviour. In these studies, cf. Ref. [8], the shape of fluid molecule was identified as the main parameter that controls crystallisation through the promotion or prevention of internal ordering.

4.2. Impact of ionic liquid pressurisation

In addition to the impact of different confinement gaps, the effect of IL pressurisation was studied, while the inter−plate distance was kept constant. More specifically, a gap of d_z=27 Å was used, while different pressures p_{ext} = 0, 120 and 250 kPa were applied, using the approach described in Section 2.2.

Through observation of Fig. 9(B)–(D), it can be seen that the application of external pressure prevents the wetting of the side walls of the top plate and leads to a distinct crystallisation of the unconfined IL. On the other hand, the ion density profiles inside the confinement zone are moderately influenced.

The friction results for increasing values of applied pressure are consistent with the observations in the previous subsection, with specific friction decreasing as the order of the IL increases. It can be seen that for high external pressure, i.e., p_{ext} = 250 kPa, the slope of the specific friction curve almost vanishes.

Fig. 8(C) shows that for p_{ext} = 120 kPa the local cubic structure

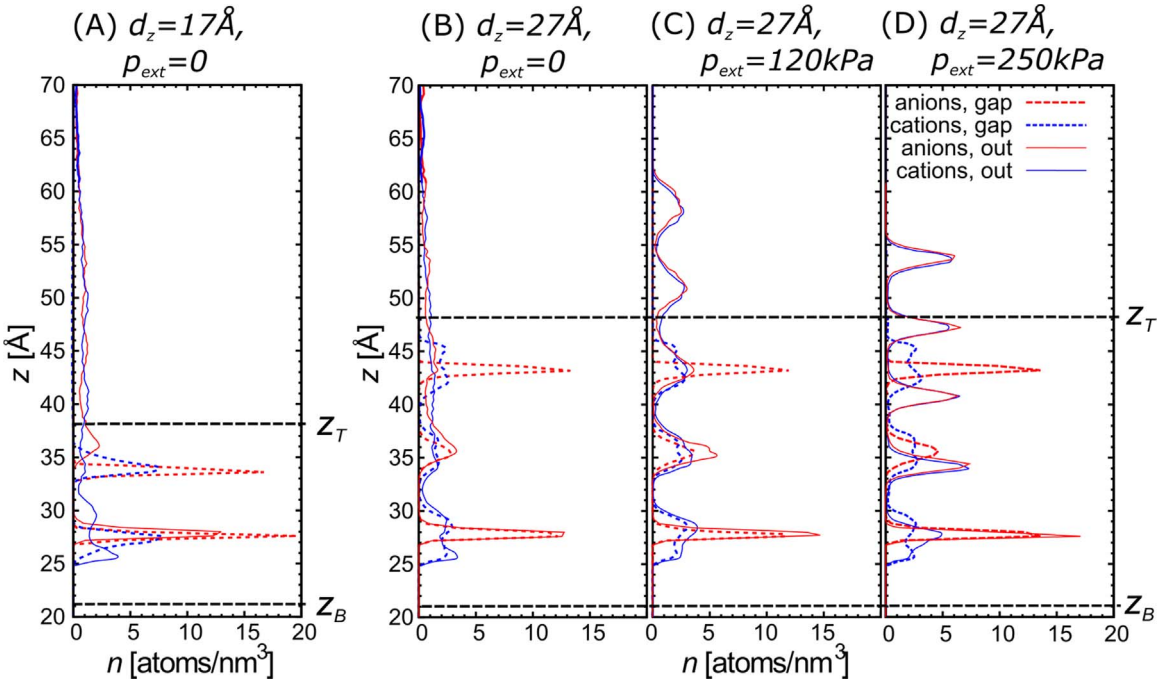

Fig. 9. Density distributions of ions along the z-axis inside (dashed lines) and outside (solid lines) the confinement zone between the solid plates for configurations shown in Fig. 8. The position of the atomic centres of the innermost layer of the top and bottom plate is denoted with z_T and z_B, respectively. Bottom plate is fixed with z_B = 21 Å.

induced by confinement between the plates served as a nucleus for further crystallisation between the plates and a well ordered single crystallite was formed in this region. Outside the confinement zone another crystallite was formed with a different orientation. Further increase of external pressure to p_{ext} = 250 kPa forced the IL in the void space to crystallise, while at the same time the IL in the confinement zone was converted to a number of smaller crystallites, cf. Fig. 8(D) and 9(D).

The reported results show a dual nature of IL lubrication, with EHL characteristics at low to medium pressures and confinement gaps that allow more than two distinct anion/cation pair layers to form. At higher pressures and smaller distances which can be translated as mixed lubrication conditions the IL is transformed to a solid-like body, while specific friction decreases to low values which are independent of the sliding velocity. This behaviour can be beneficial in engineering applications such as the piston ring–cylinder liner system, where it can be assumed that the IL crystallisation can potentially aid in preventing the solid contact between the surfaces, along with the associated high friction and wear.

5. Conclusions

In the current study we have implemented a MD simulation setup in order to study the behaviour of model ionic liquids confined between plates which are in close proximity while being in relative motion. Our MD setup was developed in a way that allows the meso–scopic study of the lubrication processes in automotive applications such as the piston ring – cylinder liner interaction inside the internal combustion engine. More specifically, our geometry was selected in order to allow a variable lubricant confinement gap combined with a varying lubricant quantity in the gap, while avoiding the squeeze-out of the lubricant into vacuum. Odd-number layering and near-wall solidification was observed between the solid plates, similar to published experimental findings. Our friction simulations have uncovered an interesting behaviour of ILs, with a logarithmic dependence of specific friction on velocity hinting at elasto-hydrodynamic lubrication at low loads. This behaviour completely changed under more critical conditions of high load, with specific friction decreasing to lower values and becoming independent of sliding velocity. This behaviour was strongly correlated with the internal structure of the IL and can provide guidance for implementing lubrication concepts that can lead to friction reduction in internal combustion engines.

Acknowledgements

The work of I.S. and M.D. was supported in part by the Serbian Ministry of Education, Science and Technological Development under Project No. OI171017 and by COST Action MP1303. Numerical simulations were run on both the HPC facilities of the Advanced Technology Division in Toyota Motor Europe and the PARADOX supercomputing facility at the Scientific Computing Laboratory of the Institute of Physics Belgrade.

References

[1] K. Holmberg, P. Andersson, A. Erdemir, Global energy consumption due to friction in passenger cars, Tribol Int 47 (2012) 221–234. http://dx.doi.org/10.1016/j.triboint.2011.11.022.

[2] B. Bhushan, J.N. Israelachvili, U. Landman, Nanotribology: friction, wear and lubrication at the atomic scale, Nature 374 (6523) (1995) 607–616. http://dx.doi.org/10.1038/374607a0.

[3] S.-J. Heo, S.B. Sinnott, D.W. Brenner, J.A. Harrison, Computational modeling of nanometer-scale tribology, in: B. Bhushan (Ed.)Nanotribology and nanomechanics: an introduction, Springer, Berlin, Heidelberg, 2005, pp. 623–691. http://dx.doi.org/10.1007/3-540-28248-3_13.

[4] S. Loehle, C. Matta, C. Minfray, T. Le Mogne, J.-M. Martin, R. Iovine, Y. Obara, R. Miura, A. Miyamoto, Mixed lubrication with C18 fatty acids: effect of unsaturation, Tribol Lett 53 (1) (2014) 319–328. http://dx.doi.org/10.1007/s11249-013-0270-3.

[5] A.C.F. Mendonça, A.A.H. Pádua, P. Malfreyt, Nonequilibrium molecular simulations of new ionic lubricants at metallic surfaces: prediction of the friction, J Chem Theory Comput 9 (3) (2013) 1600–1610. http://dx.doi.org/10.1021/ct3008827.

[6] Heyes DM, Smith ER, Dini D, Spikes HA, Zaki TA. Pressure dependence of confined liquid behavior subjected to boundary-driven shear. J. Chem. Phys. Vol. 136 (13). ⟨http://dx.doi.org/10.1063/1.3698601⟩.

[7] C. Gattinoni, D.M. Heyes, C.D. Lorenz, D. Dini, Traction and nonequilibrium phase behavior of confined sheared liquids at high pressure, Phys Rev E 88 (2013) 052406. http://dx.doi.org/10.1103/PhysRevE.88.052406.

[8] L. Martinie, P. Vergne, Lubrication at extreme conditions: a discussion about the limiting shear stress concept, Tribology Lett 63 (2) (2016) 21. http://dx.doi.org/10.1007/s11249-016-0709-4.

[9] N. Voeltzel, A. Giuliani, N. Fillot, P. Vergne, L. Joly, Nanolubrication by ionic

liquids: molecular dynamics simulations reveal an anomalous effective rheology, Phys Chem Chem Phys 17 (2015) 23226–23235. http://dx.doi.org/10.1039/C5CP03134F.

[10] J. Gao, W.D. Luedtke, D. Gourdon, M. Ruths, J.N. Israelachvili, U. Landman, Frictional forces and Amontons'law: from the molecular to the macroscopic scale, J Phys Chem B 108 (11) (2004) 3410–3425. http://dx.doi.org/10.1021/jp036362l.

[11] M.O. Robbins, M.H. Müser, Computer simulations of friction, lubrication, and wear, in: B. Bhushan (Ed.)Modern tribology handbook, two volume set, mechanics & materials Science, CRC Press, Boca Roton, 2000. http://dx.doi.org/10.1201/9780849377877.ch20.

[12] R.E. Rudd, J.Q. Broughton, Coarse-grained molecular dynamics and the atomic limit of finite elements, Phys Rev B 58 (1998) R5893–R5896. http://dx.doi.org/10.1103/PhysRevB.58.R5893.

[13] Y. Wang, W. Jiang, T. Yan, G.A. Voth, Understanding ionic liquids through atomistic and coarse-grained molecular dynamics simulations, Acc Chem Res 40 (11) (2007) 1193–1199. http://dx.doi.org/10.1021/ar700160p.

[14] M.-D. Bermúdez, A.-E. Jiménez, J. Sanes, F.-J. Carrión, Ionic liquids as advanced lubricant fluids, Molecules 14 (8) (2009) 2888–2908. http://dx.doi.org/10.3390/molecules14082888.

[15] K. Mistry, M.F. Fox, M. Priest, Lubrication of an electroplated nickel matrix silicon carbide coated eutectic aluminium-silicon alloy automotive cylinder bore with an ionic liquid as a lubricant additive, Proc Inst Mech Eng, Part J: J Eng Tribol 223 (3) (2009) 563–569. http://dx.doi.org/10.1243/13506501JET562.

[16] J. Qu, D.G. Bansal, B. Yu, J.Y. Howe, H. Luo, S. Dai, H. Li, P.J. Blau, B.G. Bunting, G. Mordukhovich, D.J. Smolenski, Antiwear performance and mechanism of an oil-miscible ionic liquid as a lubricant additive, ACS Appl Mater Interfaces 4 (2) (2012) 997–1002. http://dx.doi.org/10.1021/am201646k.

[17] J. Qu, P.J. Blau, S. Dai, H. Luo, H.M. Meyer, Ionic liquids as novel lubricants and additives for diesel engine applications, Tribology Lett 35 (3) (2009) 181–189. http://dx.doi.org/10.1007/s11249-009-9447-1.

[18] O.Y. Fajardo, F. Bresme, A.A. Kornyshev, M. Urbakh, Electrotunable friction with ionic liquid lubricants: how important is the molecular structure of the ions?, J Phys Chem Lett 6 (20) (2015) 3998–4004. http://dx.doi.org/10.1021/acs.jpclett.5b01802.

[19] Fajardo O, Bresme F, Kornyshev A, Urbakh M. Electrotunable lubricity with ionic liquid nanoscale films. Scientific reports 5.⟨http://dx.doi.org/10.1038/srep07698⟩.

[20] A.E. Somers, P.C. Howlett, D.R. MacFarlane, M. Forsyth, A review of ionic liquid lubricants, Lubricants 1 (1) (2013) 3. http://dx.doi.org/10.3390/lubricants1010003.

[21] Capozza R, Vanossi A, Benassi A, Tosatti E. Squeezout phenomena and boundary layer formation of a model ionic liquid under confinement and charging. J. Chem. Phys. Vol. 142 (6). ⟨http://dx.doi.org/10.1063/1.4907747⟩.

[22] F. Varnik, L. Bocquet, J.-L. Barrat, L. Berthier, Shear localization in a model glass, Phys Rev Lett 90 (2003) 095702. http://dx.doi.org/10.1103/PhysRevLett.90.095702.

[23] A.V. Mokshin, J.-L. Barrat, Shear-induced crystallization of an amorphous system, Phys Rev E 77 (2008) 021505. http://dx.doi.org/10.1103/PhysRevE.77.021505.

[24] F. Federici Canova, H. Matsubara, M. Mizukami, K. Kurihara, A.L. Shluger, Shear dynamics of nanoconfined ionic liquids, Phys Chem Chem Phys 16 (2014) 8247–8256. http://dx.doi.org/10.1039/C4CP00005F.

[25] S. Plimpton, Fast parallel algorithms for short-range molecular dynamics, J Comput Phys 117 (1) (1995) 1–19. http://dx.doi.org/10.1006/jcph.1995.1039.

[26] J. Gao, W.D. Luedtke, U. Landman, Layering transitions and dynamics of confined liquid films, Phys Rev Lett 79 (1997) 705–708. http://dx.doi.org/10.1103/PhysRevLett.79.705.

[27] D.J. Hardy, J.E. Stone, K. Schulten, Multilevel summation of electrostatic potentials using graphics processing units, Parallel Comput 35 (3) (2009) 164–177. http://dx.doi.org/10.1016/j.parco.2008.12.005.

[28] M.S. Daw, M.I. Baskes, Embedded-atom method: derivation and application to impurities, surfaces, and other defects in metals, Phys Rev B 29 (12) (1984) 6443. http://dx.doi.org/10.1103/PhysRevB.29.6443.

[29] I. Stankovic, S. Hess, M. Kröger, Structural changes and viscoplastic behavior of a generic embedded-atom model metal in steady shear flow, Phys Rev E 69 (2) (2004) 021509. http://dx.doi.org/10.1103/PhysRevE.69.021509.

[30] A. Gubbels-Elzas, B.J. Thijsse, Ionic motion during field-assisted oxidation of aluminium studied by molecular dynamics simulations, Comput Mater Sci 90 (2014) 196–202. http://dx.doi.org/10.1016/j.commatsci.2014.03.062.

[31] F. Iori, S. Corni, Including image charge effects in the molecular dynamics simulations of molecules on metal surfaces, J Comput Chem 29 (10) (2008) 1656–1666. http://dx.doi.org/10.1002/jcc.20928.

[32] S. Perkin, Ionic liquids in confined geometries, Phys Chem Chem Phys 14 (2012) 5052–5062. http://dx.doi.org/10.1039/C2CP23814D.

[33] R. Hayes, N. Borisenko, M.K. Tam, P.C. Howlett, F. Endres, R. Atkin, Double layer structure of ionic liquids at the Au(111) electrode interface: an atomic force microscopy investigation, J Phys Chem C 115 (14) (2011) 6855–6863. http://dx.doi.org/10.1021/jp200544b.

[34] A.M. Smith, K.R. Lovelock, N.N. Gosvami, T. Welton, S. Perkin, Quantized friction across ionic liquid thin films, Phys Chem Chem Phys 15 (37) (2013) 15317–15320. http://dx.doi.org/10.1039/C3CP52779D.

[35] P.D. Kaplan, J.L. Rouke, A.G. Yodh, D.J. Pine, Entropically driven surface phase separation in binary colloidal mixtures, Phys Rev Lett 72 (4) (1994) 582–585. http://dx.doi.org/10.1103/PhysRevLett.72.582.

[36] S. Bair, L. Martinie, P. Vergne, Classical EHL versus quantitative EHL: a perspective part II – super-arrhenius piezoviscosity, an essential component of elastohydrodynamic friction missing from classical EHL, Tribol Lett 63 (3) (2016) 37. http://dx.doi.org/10.1007/s11249-016-0725-4.

Theoretical and Experimental Study of Helices Composed of Spherical Dipoles

Miljan Dašić[a], Igor Stanković[a]

[a]*Scientific Computing Laboratory, Institute of Physics Belgrade, University of Belgrade*

Abstract. Tubular and cylindrical lattices are principal structural elements in biological systems. They give rise to structures, such as bacterial flagella and microtubules, which are essential building blocks of cells. The complexity of the structures formed by the particles with dipole-dipole interaction is a result of the interplay between anisotropic near-field interaction and long-range influence of the global geometry of the structure. Subject of this paper is the investigation of infinite 3D structures, i. e. tubes and helices. We will show that tubes are in terms of structure, actually a subset of helices. There is an endless number of different helical configurations. Nevertheless, densely packed structures exist in a number of well defined points in parameter space. We observe a structural similarity of, so called, Z-tubes, with the structures in typical experimental images of microtubules. These tubes can be decomposed into chains which are analogous to biological filaments, of which microtubules are made of. We present a way of geometric generation of densely packed helical structures composed of hard spheres. Later on, we show how to assign dipole moments to the particles making up those structures, in order to obtain dipole orientations which follow the geometry. Experimental study has proved that structures with such dipole orientations are stable.

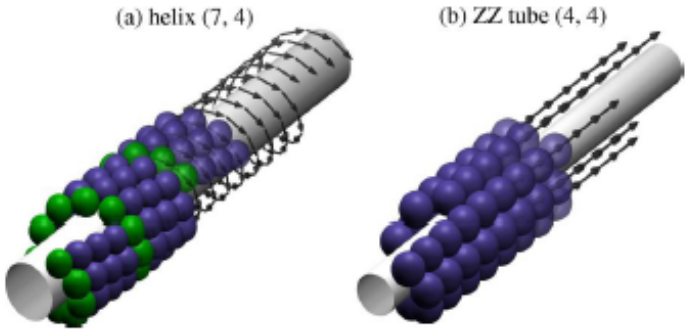

FIGURE 1. Ilustration of one representative four-stranded helix (i. e. having ST dipole orientation) (a) and one representative ZZ tube (b).

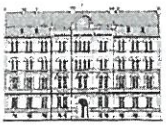

Република Србија
Универзитет у Београду
Физички факултет
Д.Бр.2014/8004
Датум: 31.10.2014. године

На основу члана 161 Закона о општем управном поступку и службене евиденције издаје се

УВЕРЕЊЕ

Дашић (Драган) Миљан, бр. индекса 2014/8004, рођен 03.11.1990. године, Параћин, Република Србија, уписан школске 2014/2015. године, у статусу: финансирање из буџета; тип студија: докторске академске студије; студијски програм: Физика.

Према Статуту факултета студије трају (број година): три.
Рок за завршетак студија: у двоструком трајању студија.

Ово се уверење може употребити за регулисање војне обавезе, издавање визе, права на дечији додатак, породичне пензије, инвалидског додатка, добијања здравствене књижице, легитимације за повлашћену вожњу и стипендије.

Овлашћено лице факултета

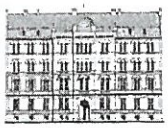

Република Србија
Универзитет у Београду
Физички факултет
Д.Бр.2014/8004
Датум: 31.10.2014. године

На основу члана 161 Закона о општем управном поступку и службене евиденције издаје се

УВЕРЕЊЕ

Дашић (Драган) Миљан, бр. индекса 2014/8004, рођен 03.11.1990. године, Параћин, Република Србија, уписан школске 2014/2015. године, у статусу: финансирање из буџета; тип студија: докторске академске студије; студијски програм: Физика.

Према Статуту факултета студије трају (број година): три.
Рок за завршетак студија: у двоструком трајању студија.

Ово се уверење може употребити за регулисање војне обавезе, издавање визе, права на дечији додатак, породичне пензије, инвалидског додатка, добијања здравствене књижице, легитимације за повлашћену вожњу и стипендије.

Овлашћено лице факултета

Република Србија

УБ

Универзитет у Београду
Електротехнички факултет, Београд

Оснивач: Република Србија
Дозволу за рад број 612-00-02666/2010-04 од 10. децембра 2010.
године је издало Министарство просвете и науке Републике Србије

Диплома

Мильан, Драган, Дашић

рођен 3. новембра 1990. године у Параћину, Република Србија, уписан школске 2009/2010. године, а дана 5. јула 2013. године завршио је основне академске студије, првог степена, на студијском програму Електротехника и рачунарство, обима 240 (двеста четрдесет) бодова ЕСПБ са просечном оценом 9,93 (девет и 93/100).

На основу тога издаје му се ова диплома о стеченом високом образовању и стручном називу

дипломирани инжењер електротехнике и рачунарства

Број: 1774200
У Београду, 19. новембра 2013. године

Декан
Проф. др Бранко Ковачевић

Ректор
Проф. др Владимир Бумбаширевић

00017866

Република Србија

УБ

Универзитет у Београду
Електротехнички факултет, Београд

Оснивач: Република Србија
Дозволу за рад број 612-00-02666/2010-04 од 10. децембра 2010.
године је издало Министарство просвете и науке Републике Србије

Диплома

Миљан, Драган, Дашић

рођен 3. новембра 1990. године у Параћину, Република Србија, уписан школске 2013/2014. године, а дана 16. јула 2014. године завршио је мастер академске студије, другог степена, на студијском програму Електротехника и рачунарство, обима 60 (шездесет) бодова ЕСПБ са просечном оценом 10,00 (десет и 0/100).

На основу тога издаје му се ова диплома о стеченом високом образовању и академском називу

мастер инжењер електротехнике и рачунарства

Број: 3427800
У Београду, 20. јануара 2015. године

Декан
Проф. др Бранко Ковачевић

Ректор
Проф. др Владимир Бумбаширевић

00034384

Научном већу Института за физику у Београду
Београд, 21. април 2017. године

Кратак преглед научне активности кандидата

Миљан Дашић је запослен у Лабораторији за примену рачунара у науци, која припада Националном центру изузетних вредности за изучавање комплексних система Института за физику у Београду и ангажован је на пројекту основних истраживања Министарства просвете, науке и технолошког развоја Републике Србије ОН171017, под називом "Моделирање и нумеричке симулације сложених вишечестичних физичких система". На поменутом пројекту ради на темама у вези са истраживањем структуре и динамичког понашања просторно ограничених диполних и јонских система, под менторством др Игора Станковића.

У оквиру свог досадашњег рада, Миљан Дашић је радио на истраживању диполних структура туба и хеликса формираних од чврстих диполних сфера са сталним диполним моментом. Кандидат је имплементирао директно сумирање дипол-дипол интеракције за рачунање кохезионе енергије коначних структура, као и Лекнеров метод за сумирање дипол-дипол интеракције за 1D бесконачне периодичне структуре. На основу геометријских параметара направио је преглед различитих класа тубуларних и хеликоидних диполних структура и потом је извео изразе за површинску густину паковања за случај свих класа туба и за општи случај вишеструко намотаних густо пакованих хеликса. Спровео је статичку анализу и добио да кохезиона енергија немонотоно зависи од густине паковања при компресији хеликса и порасту њихове густине паковања. Ради детаљног описа испитиваних структура, уведени су адекватни параметри уређења који описују различите режиме уређења ових структура. Конкретно, кандидат је радио на развоју симулација за генерисање диполних структура и прорачун њихове кохезионе енергије, као и за прорачун параметара попут површинске густине паковања, оријентације дипола и уведених параметара уређења. Такође, радио је на визуелизацији репрезентативних структура. Резултат тог ангажмана је рад **"Structure and cohesive energy of dipolar helices"** објављен јануара 2016. године у врхунском међународном часопису *Soft Matter*.

Друга тема је моделовање јонских течности методом молекуларне динамике са циљем њихове примене као лубриканта у аутомобилској индустрији. Миљан Дашић је у периоду од 5. октобра 2015. до 8. априла 2016. године био ангажован на пракси у Одељењу за напредне технологије Техничког Центра компаније "Toyota Motor Europe", у Завентему (Белгија). По повратку на Институт за физику, наставио је рад на истом пројекту. Циљ пројекта је развој модела који ће укључити све релевантне физичке процесе везане за подмазивање контакта прстена клипа и зидова цилиндра у аутомобилском мотору. Кандидатов допринос односи се на развој модела и његову софтверску имплементацију, као и на визуелизацију резултата симулација. Резултат тог ангажмана је учешће на међународној конференцији Лидс-Лион у септембру 2016. године и рад **"Molecular dynamics investigation of a model ionic liquid lubricant for automotive applications"** објављен децембра 2016. године у врхунском међународном часопису *Tribology International*. Ово је пример успешно остварене сарадње домаће институције са врхунском светском компанијом као што је Тојота. Овим ангажманом је дат пример примене теоријских знања на реалне проблеме, од интереса у аутомобилској индустрији.

Тренутно ради на анализи диполних структура формираних у равни, у присуству спољашњег поља. Наставио је рад на симулацијама молекуларне динамике са унапређеним моделом јонске течности.

	ДОКТОРСКЕ СТУДИЈЕ		

ПРЕДЛОГ ТЕМЕ ДОКТОРСКЕ ДИСЕРТАЦИЈЕ КОЛЕГИЈУМУ ДОКТОРСКИХ СТУДИЈА

Школска година 2016/2017

Подаци о студенту

Име: Милован

Презиме: Дашић

Број индекса: 8004/2014

Научна област дисертације: ФИЗИКА КОНДЕНЗОВАНЕ МАТЕРИЈЕ И СТАТИСТИЧКА ФИЗИКА

Подаци о ментору докторске дисертације

Име: Игор

Презиме: Станковић

Научна област: ФИЗИКА КОНД. МАТЕРИЈЕ И СТАТИСТИЧКА ФИЗИКА

Звање: ВИШИ НАУЧНИ САРАДНИК

Институција: ИНСТИТУТ ЗА ФИЗИКУ БЕОГРАД

Предлог теме докторске дисертације

Наслов

САМООРГАНИЗАЦИЈА И ДИНАМИЧКО ПОНАШАЊЕ ПРОСТОРНО ОГРАНИЧЕНИХ ДИСИПАТИВНИХ И ЖИВИХ СИСТЕМА

Уз пријаву теме докторске дисертације Колегијуму докторских студија, потребно је приложити следећа документа:

1. Семинарски рад (дужине до 10 страница)
2. Кратку стручну биографију писану у трећем лицу једнине
3. Фотокопију индекса са докторских студија

Потпис ментора

Датум 18/04/2017

Потпис студента

Мишљење Колегијума докторских студија

Након образложења теме докторске дисертације Колегијум докторских студија је тему

прихватио ☒ није прихватио ☐

Датум

19.04.2017

Продекан за науку Физичког факултета